

STIS Longslit Spectroscopy Of The Narrow Line Region Of NGC 4151. I. Kinematics and Emission Line Ratios¹

C. H. Nelson², D. Weistrop², J. B. Hutchings³, D. M. Crenshaw⁴, T. R. Gull⁵, M. E. Kaiser⁶, S. B. Kraemer⁴, D. Lindler⁵

ABSTRACT

Longslit spectra of the Seyfert galaxy NGC 4151 from the UV to near infrared have been obtained with STIS to study the kinematics and physical conditions in the NLR. The kinematics show evidence for three components, a low velocity system in normal disk rotation, a high velocity system in radial outflow at a few hundred km s⁻¹ relative to the systemic velocity and an additional high velocity system also in outflow with velocities up to 1400 km s⁻¹, in agreement with results from STIS slitless spectroscopy (Hutchings *et al.*, 1998, Kaiser *et al.*, 1999, Hutchings *et al.*, 1999) We have explored two simple kinematic models and suggest that radial outflow in the form of a wind is the most likely explanation. We also present evidence indicating that the wind may be decelerating with distance from the nucleus.

We find that the emission line ratios along our slits are all entirely consistent with photoionization from the nuclear continuum source. A decrease in the [OIII] λ 5007 / H β and [OIII] λ 5007 / [OII] λ 3727 ratios suggests that the density decreases with distance from the nucleus. This trend is borne out by the [SII] ratios as well. We find no strong evidence for interaction between the radio jet and the NLR gas in either the kinematics or the emission line ratios in agreement with the results of Kaiser *et al.* (1999) who find no spatial coincidence of NLR clouds and knots in the radio jet. These results are in contrast to other recent studies of nearby AGN which find evidence for significant interaction between the radio source and the NLR gas.

Subject headings: galaxies: Seyfert, galaxies: individual (NGC 4151), galaxies: kinematics and dynamics, line: formation

1. Introduction

Since the launch of the Hubble Space Telescope (HST) many imaging studies of the Narrow Line Regions (NLR) of active galactic nuclei (AGN) have been carried out. These studies have shown that the emission line gas often has a complex morphology, frequently taking the form of a bicone centered on the galaxy nucleus. (*e.g.* NGC 4151, Evans *et al.*, 1993, Boksenberg *et al.* 1995, NGC 1068, Evans *et al.* 1991, see also the archival study by Schmitt & Kinney 1996). In the standard model for an AGN, a dense molecular torus with a radius of a few parsecs surrounds the nucleus and collimates the radiation field (*e.g.* Antonucci 1993). According to the model, differences in the continuum and emission line spectra, which form the basis for classification of Seyferts and other

¹Based on observations with the NASA/ESA *Hubble Space Telescope*, obtained at the Space Telescope Science Institute, which is operated by AURA Inc under NASA contract NAS5-26555

²Physics Dept., University of Nevada, Las Vegas, Box 4002, 4505 Maryland Pkwy., Las Vegas, NV 89154, cnelson@physics.unlv.edu, weistrop@nevada.edu

³Dominion Astrophysical Observatory, National Research Council of Canada, 5071 W. Saanich Rd., Victoria B.C. V8X 4M6, Canada

⁴Catholic University of America, NASA/Goddard Space Flight Center, Code 681, Greenbelt, MD 20771

⁵NASA/Goddard Space Flight Center, Code 681, Greenbelt, MD 20771

⁶Department of Physics and Astronomy, Johns Hopkins University, Baltimore, MD 21218

types of AGN, can be explained largely by differences in the orientation of the torus to our line of sight. For example, in type 1 Seyfert galaxies our viewing angle is close to the symmetry axis of the torus allowing a direct view of the Broad Line Region (BLR) and the nuclear continuum source, while in type 2 Seyfert galaxies our vantage point lies closer to the plane of the torus which then blocks a direct view of the inner regions.

In many instances the NLR morphology and kinematics appear closely linked to the radio structure, particularly in Seyfert galaxies with linear or jet-like radio sources. In these objects the line emitting gas is often found to be cospatial with the radio jets and there is also kinematic evidence for physical interaction between the jets and the NLR gas (Capetti *et al.* 1999, Whittle *et al.*, 1988). The suggestion has been made that expansion of the radio plasma into the host galaxy's interstellar medium produces fast shock waves which emit a hard continuum and ultimately provide the dominant source of ionizing photons (Taylor, Dyson, & Axon, 1992, Sutherland, Bicknell & Dopita, 1993).

The degree to which photoionization by a nuclear continuum source or by autoionizing shocks contributes to the overall energetics of the NLR has been the subject of some debate. In principal one can distinguish between them spectroscopically by studying the spatially resolved kinematics and the physical conditions of the gas as revealed by the relative intensities of specific emission lines. The Space Telescope Imaging Spectrograph (STIS) is ideally suited for this type of study. We have therefore undertaken a detailed investigation of the kinematics and physical conditions across the NLR of NGC 4151, one of the nearest Seyfert galaxies.

Evidence for outflow and photo-ionization cones in the NLR of NGC 4151 was presented by Schulz (1988, 1990) based on ground-based longslit spectroscopy. Peculiar flat-topped and double-peaked emission line profiles were observed to the SE and NW between $2''$ and $6''$ from the nucleus and are most consistent with outflow models. Schulz (1990) suggests that the outflow is driven either by a wind related to the active nucleus or by an expanding radio plasmon.

The NLR kinematics in NGC 4151 have been studied in detail using slitless spectroscopy from STIS (Hutchings *et al.*, 1998, Kaiser *et al.*, 1999,

and Hutchings *et al.*, 1999). These observations reveal three distinct kinematic components: one consisting of low velocity clouds ($|V - V_{sys}| \sim 100 \text{ km s}^{-1}$), primarily in the outer NLR following the rotation of the host galaxy disk, a second consisting of moderately high velocity clouds ($|V - V_{sys}| \geq 400 \text{ km s}^{-1}$) most likely associated with radial outflow within the biconical morphology and a third component of fainter but much higher velocity clouds ($|V - V_{sys}| \sim 1400 \text{ km s}^{-1}$) which is also outflowing but not restricted to the biconical flow of the intermediate velocity component. No evidence for higher velocities in the vicinity of the radio knots was found suggesting that the radio jet has minimal influence on the NLR kinematics.

A somewhat different conclusion was drawn by Winge *et al.* (1999) primarily using longslit spectroscopy with HST's Faint Object Camera. They claim evidence for strong interaction between the radio jet and the NLR gas. Furthermore, after subtracting the influence of the radio jet and galaxy rotation on the kinematics, they suggest that the residual motion is the rotation of a thin disk of gas on nearly Keplerian orbits beyond $0''.5$ (60 pc using their linear scale) around an enclosed mass of $10^9 M_{\odot}$. Interior to 60 pc the velocities turn over suggesting that the mass is extended, and, if their interpretation is correct, they are able to place upper limits on the mass of a nuclear black hole of $\sim 5 \times 10^7 M_{\odot}$.

In this paper we present the initial results from our low resolution, longslit spectroscopy. A second paper presents a detailed photoionization model using the emission line ratios presented here (Kraemer *et al.* 1999, Paper II). Section 2 presents the observations and describes the data reduction procedures including correction for scattered light from the Seyfert nucleus. Section 3 describes the results of the kinematic and preliminary line ratio analyses. In section 4 we discuss the results in terms of different NLR models. We summarize our results and conclusions in section 5.

2. Observations and Data Reduction

Longslit spectroscopy of NGC 4151 was obtained with STIS on board HST. Four low dispersion gratings, G140L, G230LB, G430L and G750L, were used producing spectra ranging from the UV

at 1150 Å to the near-infrared at 10,270 Å. Note that the G230LB mode, which uses the CCD detector, was used instead of the G230L, due to the bright object protection limits imposed on use of the MAMA detectors. Two slit alignments were chosen to cover regions of specific interest and as many of the bright emission line clouds as possible. The first position was chosen to pass through the nucleus at position angle 221°, while the second was offset from the nucleus by 0".1 to the south at position angle 70°. Figure 1 shows the slit apertures drawn on the WFPC-2 narrow band image of the [OIII] λ 5007 emission line structure obtained from the HST archives (proposal ID 5124, principal investigator H. Ford). The 0".1 slit was used to preserve spectral resolution, given here for each of the four gratings assuming an extended source (the emission line clouds are generally resolved along the slit): 2.4 Å for G140L, 2.7 Å for G230LB, 5.5 Å for G430L, and 9.8 Å for G750L (Woodgate *et al.* 1998, Kimble *et al.* 1998, Baum *et al.* 1998). A log of the observations is presented in Table 1. One set of observations failed and as a result no G140L spectrum was available for P.A. 70°.

The spectra were reduced using the IDL software developed at NASA’s Goddard Space Flight Center for the Instrument Definition Team (Lindler *et al.* 1998). Cosmic ray hits were identified and removed from observations using the CCD detector (G230LB, G430L, and G750L) by combining the multiple images obtained at each visit in each spectroscopic mode. Hot or warm pixels (identified in STIS dark images) were replaced by interpolation in the dispersion direction. Wavelength calibration exposures obtained after each science observation were used to correct the wavelength scale for zero-point shifts. The spectra were also geometrically rectified and flux-calibrated to produce a constant wavelength along each column (the spatial direction) and fluxes in units of $\text{ergs s}^{-1} \text{cm}^{-2} \text{Å}^{-1}$ per cross-dispersion pixel. Spectra obtained at the same position angle and spectroscopic mode were combined to increase the signal-to-noise ratios.

The bright, unresolved Seyfert nucleus of NGC 4151 creates a number of difficulties when trying to examine emission lines from the NLR close in. Scattered light, largely from Airy rings imaged on the slit, causes features of the nuclear point source

spectrum to be superimposed on fainter NLR features. These follow linear tracks running nearly parallel to the dispersion, diverging slightly with wavelength and can be detected as much as 20–30 pixels from the nucleus (Bowers & Baum, 1998). This is a particularly difficult problem for measuring the Balmer lines in the NLR since the BLR lines are strong and often have peculiar shapes which can influence the continuum placement if not subtracted properly. In addition, the extended halo of the PSF must be modeled and subtracted. Furthermore, reflection of the bright nucleus in the CCD modes appears as a ghost spectrum, which is displaced from the nucleus in both the dispersion and spatial directions. Several techniques were used to remove these effects.

Corrections for scattered light in the spectra were applied in the following order: 1) removal of the reflection spectrum (in the CCD spectra), 2) correction for the halo, and 3) removal of the remaining PSF, including the diffraction-ring tracks. The reflection spectrum is not only shifted in both directions, it is broadened in the spatial direction, compressed in the dispersion direction, and altered in intensity as a function of wavelength (it tends to be redder than the nuclear spectrum). The reflection in each original spectral image was isolated by subtracting the scattered-light at the same spatial distances on the other side of the nuclear spectrum. Then the nuclear spectrum was shifted along the slit and compressed in the dispersion direction until the strong emission features matched those in the reflection. It was then divided into the observed reflection to obtain the large-scale intensity variations in both dispersion and spatial directions. These variations were fitted in wavelength regions that do not contain extended emission, in both directions with low-order splines. The fits were then multiplied by the altered nuclear spectrum to produce a model of the reflection which was subtracted from the original spectral image. A circularly-symmetric halo was adopted from previous work on the STIS detectors (Lindler 1999), and collapsed to match the observed PSF in the spatial direction (obtained by adding regions along the dispersion direction that do not contain extended emission). The halo function was adjusted at various radial positions until a reasonable match was obtained with the broad-scale profile of the PSF (i.e., ignoring diffraction

tracks, etc.). The halo was then deconvolved from the original image using an iterative technique that removes flux from the halo and places it in the core.

To remove the remaining scattered light, a scattering template was constructed using archival observations of stars observed with the same grating and slit width. First, the template spectrum was normalized in the dispersion direction by dividing through by the spectrum summed along the slit. Next, the template was smoothed in the dispersion direction, using a median filter with a 50 pixel wide window. The nuclear spectrum of NGC 4151 was then multiplied into the template to simulate the scattered light spectrum. The scattering subtracted spectra are clean of broad line emission as close as 4 pixels from the nucleus. Because the nuclear $H\alpha$ line in the G750L spectrum at P.A. 221 is saturated, the true line profile is distorted and complicates construction of the scattering template. A substitute for the saturated profile was obtained from the G750M short exposure in our slitless spectroscopy with good results.

An alternative approach was also applied which used the structure along the slit in a continuum region of the NGC 4151 spectrum itself to form the model template. First, the entire image was normalized by dividing each row (which lies along the dispersion direction) by the summed nuclear spectrum from the central four rows. A spline (typically of order 11) was then fitted along each row in regions that do not contain emission lines. Thus the fit is a model of the scattering as a function of wavelength and position along the slit for a point source spectrum of constant flux per unit wavelength. This procedure was effective in modeling the diffraction tracks as well as the overall PSF. The spline fits were then multiplied by the nuclear spectrum at each spatial position, and subtracted from the reflection- and halo-corrected image to produce a final corrected image, which was used for subsequent analysis.

The resulting spectra are shown in Figure 2 and Figure 3. The corrections bring out the structure in the bright lines, and allow us to see fainter lines that are not evident in the original spectra. The correction process was not perfect, as evidenced by the faint structure seen in the regions above and below the strong nuclear lines, particularly $H\alpha$ λ 6563. However, these problems are minor,

and the contaminating effects of nuclear absorption and emission were removed well enough for accurate measurement of the extended emission, even very close to the nucleus.

Although our primary interest is the NLR, the data set also contains high quality nuclear spectra of NGC 4151 at two epochs. Monitoring campaigns have shown pronounced variability in both the nuclear continuum and BLR emission (Robinson *et al.*, 1994, Crenshaw *et al.*, 1996, Warwick *et al.*, 1996, Kaspi *et al.*, 1996, Ulrich *et al.*, 1997, Weymann *et al.*, 1997, Peterson *et al.* 1998). Over a time interval of 33 days (Jan. 8, 1998 and Feb. 10, 1998; see Table 1) the nuclear continuum dropped by 17% at 3050 Å and 10% at 6924 Å decreasing monotonically between these two wavelengths. This degree of variation is consistent with that reported in short timescale variability studies (Kaspi *et al.* 1996). The variation of the BLR emission lines is less pronounced than that of the continuum, with $H\gamma$ and $H\beta$ showing a decrease in flux, while the change in the $H\alpha$ + N[II] line profile is more difficult to evaluate. The absorption lines in our far-UV spectrum are similar to those in the FOS spectra published by Weymann *et al.* (1997) but is at too low a resolution for comparison to the high resolution GHRS spectrum.

3. Analysis

3.1. Measurement of Line Fluxes and Component Deblending

Emission line fluxes and their errors were measured along the slit in each spectral range for a total of 45 emission lines. Individual spectra were extracted from the longslit spectra by summing along the slit. The size of the extraction bins was dictated by the need for reasonably accurate fluxes for the He II λ 1640 and λ 4686 lines, which were used for the reddening corrections in Paper II. Experimentation revealed that bin lengths of $0''.2$ (4 CCD pixels, 8 MAMA pixels) within the inner $\pm 1''$ and $0''.4$ outside this region would provide reasonable signal-to-noise ratios for these lines, and still isolate the emission-line clouds that we identified in our earlier papers. In some cases slightly different bin sizes were used to isolate individual clouds or to increase the signal-to-noise ratios.

To measure the line fluxes, first a linear fit

to the continuum adjacent to each line was subtracted. Typically the continuum was very close to zero following removal of the scattered light, but continuum subtraction was helpful in regions of residual structure. Next, the extreme ends of the red and blue wings of the line were marked and the total flux and centroid were computed between these two points. The uncertainties in the line fluxes were estimated using the error arrays for each spectrum produced by CALSTIS and a propagation of errors analysis (Bevington, 1969). For the blended lines of $H\alpha$ and $[\text{N II}]\lambda\lambda 6548, 6584$, and $[\text{S II}]\lambda\lambda 6717, 6731$, we used the $[\text{O III}]\lambda 5007$ line as a template to deblend the lines (see Crenshaw & Peterson 1986). This was superior to Gaussian fitting since the emission line profiles are often complex. The results of the emission line flux measurements are presented in Table 2 where the flux values are listed relative to $H\beta$ and the $H\beta$ flux is given at the bottom in units of 10^{-15} ergs cm^{-2} s^{-1} \AA^{-1} . The errors obtained for each flux are given in parentheses.

Because of the failure of the far-UV spectrum at P.A. 70° no G140L spectrum was obtained and so a reddening correction using the He II lines was not possible. Although dereddening using the Balmer decrement is certainly valid, a reliable extrapolation from the red to the blue and near-UV lines is uncertain. We prefer, therefore, to continue the analysis without the corrected line ratios taking care that any possible effects of reddening are accounted for by other means. Correction of the line ratios for reddening is an important step for a detailed photoionization model and is therefore presented in Paper II for the data at P.A. 221° .

To extract information on the multiple kinematic components the $[\text{O III}]\lambda 5007$ and $[\text{O III}]\lambda 4959$ lines were fitted independently with one to three Gaussians. Many slit extractions showed two components although in only a few cases was there compelling evidence for a third. Only velocity components measured independently at both $[\text{O III}]\lambda 4959$ and $[\text{O III}]\lambda 5007$ are included. To test that each component represented the true kinematics of the gas, we compared the velocities obtained at both $[\text{O III}]\lambda 5007$ and $[\text{O III}]\lambda 4959$. Only those components with velocity difference in the two lines less than or equal to twice the mean difference for all points were retained. The pro-

cedure was then repeated. The first iteration removed velocity components that were wildly discordant, and therefore unlikely to be real, while the second gave us confidence that the remaining components are physically significant. From the difference in velocity between components extracted at $[\text{O III}]\lambda 4959$ and $[\text{O III}]\lambda 5007$, we estimate the standard deviation of the velocities to be 30 km s^{-1} . The results for each slit position are given in Table 3a and 3b where the Gaussian components are listed in order of increasing velocity. Negative slit positions correspond to the SW region and positive slit positions correspond to the NE.

3.2. Kinematics

Figure 4 shows portions of the longslit spectra centered on the $[\text{O III}]\lambda 5007$, $[\text{O III}]\lambda 4959$ and $H\beta$ emission lines for both slit positions, with the NE end of the slit at the top. The complex velocity structure that has been noted in both ground-based and HST studies (*e.g.* Schulz 1990, Kaiser *et al.* 1999, Hutchings *et al.*, 1999) is seen including line splitting at several positions along the slit. Note that as a result of our scattering correction and PSF subtraction we are able to probe the emission line kinematics to within $0''.2$ of the nucleus.

Included within our slits are four of the high velocity regions (absolute value of projected velocity greater than 400 km s^{-1}) reported in Hutchings *et al.* (1999) and 20 of the clouds identified in Kaiser *et al.* (1999) (Tables 4a, 4b). Our agreement with Hutchings' velocities is reasonable, ranging from a difference of 6 km s^{-1} for region N detected at slit P.A. 221° , to 160 km s^{-1} for region D. While some of the difference is undoubtedly due to measurement uncertainties, there may be real differences due to the portion of the high velocity regions which fall within our slit. There may also be some uncertainty due to confusion of spectral and spatial information in the slitless data. We see components of high velocity gas not specifically identified by Hutchings *et al.* (1999) on both sides of the bicone at both slit positions (Tables 3a, 3b). This gas corresponds to high velocity gas imaged by Hutchings *et al.* (1999), but for which velocities were not previously measured. The high velocity components generally account for a small fraction of the total flux in the $[\text{O III}]\lambda$ emission lines, again

in agreement with the findings of Hutchings *et al.* (1999). We find more high velocity components in slit position P.A. 70° , which is close to the radio ridge line, than we do in the P.A. 221° slit. However, there is some high velocity gas not associated with the radio emission.

Comparison of our velocities with those reported by Kaiser *et al.* (1999) is more difficult, since in several cases they reported single velocities for clouds where we find multiple velocity components. Furthermore, there are instances of extended clouds for which our slit does not sample the entire cloud. If we compare only velocities for clouds for which we find a single velocity component and average our velocities for clouds occurring in more than one extraction bin, we find the average difference in velocities is $-18 \text{ km s}^{-1} \pm 94 \text{ km s}^{-1}$, (in the sense $V(\text{this paper}) - V(\text{Kaiser } et al.)$). This difference and range is comparable to what was found for the high velocity clouds, and can be attributed to the same causes.

Figure 5 shows the velocities of the individual [OIII] components from the Gaussian deblending. Points along P.A. 221° are marked as solid points and along P.A. 70° as open symbols. The horizontal bars indicate the size of the extracted spectrum used for the measurement along the slit. Vertical error bars are omitted since the velocity uncertainties are comparable to the size of the points on the diagram (see section 3). A systemic velocity of 997 km s^{-1} has been subtracted from the data. The solid and dashed lines show results expected for our simple models described below. The results follow the velocity distribution determined from the slitless spectroscopy of Kaiser *et al.* (1999) and the plot is similar to their Figure 8, though without the extreme high velocities. The velocities at large distances from the nucleus are consistent with the rotation of the galactic disk, while closer in the velocities are strongly blue shifted SW of the nucleus and strongly redshifted to the NE.

To better understand the kinematics we consider two possibilities for the general form of the velocity field: radial outflow from the nucleus and expansion directed away from the radio axis. We adopt the basic conical geometry of the NLR of NGC 4151 as modeled by Pedlar *et al.* (1993), with the radio jet pointing 40° from the line of sight and projected onto the plane of the sky at a P.A. of 77° . After consideration of the well-

known geometry of the host galaxy (Simkin, 1975, Bosma, Ekers, & Lequeux, 1977) we require that the cone opening angle be wide enough to include our line of sight to the nucleus and also to intersect the disk of the host galaxy, since the Extended Narrow Line Region (ENLR) kinematics follow the rotation of the disk. Pedlar *et al.* (1993) estimate the opening angle to be 130° . However, Boksenberg *et al.* (1995) argue that the NLR is density bounded and the ionized gas only partially fills the cone. Therefore we choose a narrow vertex angle of 70° which is a better match to the observed NLR structure. The models are drawn schematically in Figure 6. These models are used to estimate the radial velocity as a function of projected distance from the nucleus for each slit position angle. Our purpose is not to produce a detailed match to the observed velocities of each individual cloud, but to test two ideas about general form of the NLR kinematics. Therefore, we assume that the interior of the cone is uniformly filled and note that the observed velocity distribution is not expected to be as smooth or complete as the model, reflecting the way in which the emission line clouds fill the cone.

For both the radial outflow model and the jet expansion model we consider two cases, one in which the flow has a constant velocity and one in which the flow decelerates as it moves outward. We model this decelerating flow as a $R^{-1/2}$ dependence where R in the radial flow model is distance from the nucleus and R in the jet expansion model is distance from the radio axis. This particular form of deceleration is chosen since it seems to represent the data best and is meant only to illustrate the effect. The results are plotted in Figure 7 for all four models in the form of a model longslit spectrum of a single emission line comparable to Figure 4. The slit was chosen to lie along P.A. 70° and to have a slit width of $0''.1$ as in our STIS observations. These simulated spectra were then deblended using two Gaussians at each slit position in the same manner as the real data. The velocities for the decelerating models are shown in Figure 5 as the dashed lines (one for each Gaussian component) for the case of jet expansion and the solid lines for the case of radial flow.

For the case of expansion away from the radio axis we expect both large positive and large negative velocities relative to the systemic velocity at

any given position along the slit. In the case of radial outflow, however, large positive velocities and velocities much closer to the systemic velocity will be observed on one side of the slit while on the other side, large negative velocities and velocities near the systemic velocity are expected. Since for NGC 4151 the far side of the SW cone lies close to the plane of the sky, the bulk of the flow is transverse to the line of sight, yielding radial velocities close to the systemic value, while the near side is much closer to the line of sight yielding large approaching radial velocities. Similar considerations hold for the NE cone except that the near side of the cone lies in the plane of the sky and the far side yields the large receding velocities.

We conclude that the radial outflow case gives a better match to the observed velocity distribution than the case of expansion away from the jet. In the case of a radially decelerating flow the overall envelope of the highest velocities decreases as one moves away from the nucleus much as seen in Figure 5. Although the match is not perfect it seems to follow the trend of less extreme velocities as one moves along the slit. From these simple models we cannot exclude the possibility of some motion perpendicular to the radio jet. However, it does seem likely that the flow is dominated by a radial outflow from the nucleus which slows with distance and that any contribution from expansion away from the jet is less significant.

3.3. Line Ratios and Projected Distance from the Nucleus

An understanding of the physical conditions in the NLR can be obtained by considering how various line strengths change as a function of distance from the nucleus and with respect to each other. In Paper II (Kraemer *et al.* 1999) a detailed photoionization model is developed using the emission line fluxes presented here. In the current paper we present a simpler analysis.

The ratio of [OIII] $\lambda 5007$ to $H\beta$ is well known to be sensitive to the ionization parameter $U = Q/4\pi r^2 n_e c$, where Q is the rate at which ionizing photons are emitted, r is the distance to the nucleus, n_e is the electron density, and c is the speed of light. Figure 8 shows the [OIII] $\lambda 5007$ to $H\beta$ ratio as a function of distance along the slit for both position angles. We use ratios that have not been corrected for extinction since the lines are close in

wavelength and are therefore rather insensitive to reddening. We see from the diagram that the line ratio decreases with distance in the inner 2'' and recovers somewhat at larger radii on the NE side (positive X-axis). This trend was shown in Kaiser *et al.* (1999) from the slitless spectroscopy who suggest that this apparent change in the ionization parameter with distance reflects a decrease in density.

Apart from the increase in [OIII] $\lambda 5007 / H\beta$ on the extreme NE side of P.A. 221° , there is no significant difference in the ratio between the two position angles, suggesting that while the ionization state of the gas may change moving away from the nucleus, it generally does not change laterally, *i.e.* with distance from the radio axis.

A similar trend is seen in the ratio of [OIII] $\lambda 5007$ to [OII] $\lambda 3727$, which is also sensitive to the ionization parameter. Figure 9 plots the ratio versus distance for both slit positions. Again, the line fluxes have not been corrected for extinction but the dust is most likely patchy (see Paper II) and so is not likely to influence the overall trend and merely adds scatter. Support for this comes from the fact that the trend is largely symmetric about the nucleus indicating that no large scale dust lanes pass through our aperture. Furthermore, for the slit extractions where both He II lines used for the extinction corrections are present (along P.A. 221°), the largest change in the [OIII]/[OII] ratio from dereddening was a decrease of $\sim 30\%$ (see Paper II). Therefore, to the extent that the distribution of dust is comparable along each slit position, the conclusion of a decreasing [OIII]/[OII] ratio with distance is robust.

The safest conclusion to draw from these diagrams is that the density falls off with distance as suggested by Kaiser *et al.* (1999) and confirmed in Paper II. In fact, in the inner clouds the high [OIII]/[OII] most likely results from collisional de-excitation of the O^+ ions. Although, these trends could naively be considered an indication of decreasing ionization parameter with distance from the nucleus, the more detailed investigation in Paper II suggests a more constant ionization parameter and a density which declines less rapidly than r^{-2} .

In Figure 10 the density sensitive ratio of [SII] $\lambda 6717$ to [SII] $\lambda 6731$ is plotted as a function of distance, again for both slit positions. Judging

by the size of the error bars, much of the scatter in the diagram is real suggesting that the gas is rather clumpy, with regions of higher and lower density at various points along the slit. There is also an interesting drop in the ratio very close to the nucleus particularly in the data from the P.A. 70° slit position, suggesting an increase in density there. Generally, the [SII] ratios appear to be larger farther out particularly along P.A. 221° (solid dots), indicating a decrease in density with radius, at least in the partially ionized zone. Using the five level-atom program developed by Shaw & Dufour (1995) and assuming a temperature of 15000 ° K (see below) we find that the density of the inner NLR is roughly 2000 cm⁻³ while in the outer NLR and ENLR the density has dropped to ~ 300 cm⁻³. This agrees with the results of Robinson *et al.* (1994) who found density decreasing with distance from the nucleus in NGC 4151, with an overall NLR density of 1600 cm⁻³, and a density in the ENLR of 250 cm⁻³. This is also in agreement with the interpretation of the decline in [OIII] λ5007 /Hβ as the result of a decrease in density.

The [OIII]λ5007/[OIII]λ4363 ratio is well-known to be sensitive to the temperature of the gas. Figure 11 shows the [OIII] ratio as a function of distance along the slit. The use of this ratio to calculate the temperatures is only valid for densities up to $n_e \simeq 10^5$ cm⁻³ at which point collisional de-excitation begins to have an influence on the line strengths (Osterbrock, 1974). Furthermore the [SII] densities cannot be used since they reflect densities in the partially ionized zone. Thus we use results from Paper II for the gas densities which indicate that in the O⁺⁺ zone the densities are below 10⁵cm⁻³. The results from the five-level atom program give temperatures in the range of 12000° K — 17000 ° K. Based on Figure 11 there appears to be a slight trend for a decreasing ratio (increasing temperature) with distance from the nucleus. This is difficult to confirm, however, since reddening may play a role, tending to increase the observed ratio. Paper II gives a more detailed analysis of the physical conditions along the slit.

3.4. Line Ratio Diagrams and Photoionization

Diagrams plotting one line ratio against another can be used to investigate the origin of the

photoionizing continuum. By choosing line ratios which consist of lines which are close in wavelength we can significantly reduce the effects of reddening (see *e.g.* Veilleux and Osterbrock, 1989). In Figure 12 a, b, and c, we present the optical emission line ratios [S II] λλ6717, 6731/Hα, [N II] λ6584/Hα, [O I] λ6300/Hα, respectively, plotted against [OIII] λ5007 /Hβ . In each diagram the solid line separates star-forming regions from AGN and is taken from Veilleux and Osterbrock (1989). The dashed line is the power-law photoionization model for solar abundance taken from Ferland and Netzer (1983). The ionization parameter varies from 10⁻⁴ to 10^{-1.5} from lower right to upper left.

We find that the NGC 4151 NLR clouds occupy compact regions on these diagrams indicating that the source of the ionizing continuum is the same for all of the points sampled along the slit. Thus none of the clouds observed shows evidence for star-formation or LINER-like excitation. While this result is not unexpected it is worth commenting that the NLR gas all seems to have the same source of excitation.

Other line ratio diagrams including UV lines are also interesting since they allow us to investigate the possibility of alternate ionization mechanisms for the NLR clouds (Allen *et al.* 1998). In figure 13a, b and c we plot the ratios of CIV λ1549 to He II λ1640, CIV λ1549 to CIII] λ1909, [Ne V] λ3426 to [Ne III] λ3869, respectively against [OIII] λ5007 to Hβ (only the P.A. 221° data is shown for Figures 13a and b since the far-UV observation at P.A. 70 was unsuccessful). The lines show model grids calculated using the MAPPINGS II code (Sutherland and Dopita, 1993) by Allen *et al.* (1999) for shock ionization (bottom), shock plus ionized precursor gas (middle) and for power-law photoionization (top). For the shock plus precursor models, the shock velocity increases from 200 km s⁻¹ to 500 km s⁻¹ moving from low to high [OIII] λ5007 /Hβ ratios. Notice that for the highest velocity shocks the models coincide with power-law photoionization models.

Again the NGC 4151 NLR occupies very limited regions in these diagrams corresponding to photoionization by a power law at high ionization parameter or by shock plus precursor models with very high velocity ($V_{\text{shock}} \simeq 500\text{km s}^{-1}$). These results strongly suggest that low velocity shocks play an insignificant role in accounting for

the ionization state of the NLR in NGC 4151 but we cannot rule out the possibility of ionization by radiation from fast shocks.

4. Discussion

The results of the kinematic and emission line ratio analysis can be combined to create a coherent picture of the NLR in NGC 4151. We have seen that the kinematics bear the signature of radial outflow from the nucleus and are distinctly different from an expansion away from the radio jet axis. This is an interesting result since many recent studies have reported kinematic evidence that the radio jet can have a significant influence on the motion of NLR gas (*e.g.* Bicknell *et al.* 1998, NGC 4151 Winge *et al.* 1998, Mrk 3 Capetti *et al.* 1998). In these studies the NLR gas is found immediately surrounding and expanding away from knots of radio emission as in Mrk 3 or forms a bow shock structure around the working surface of the head of the jet as in Mrk 573 (Capetti *et al.* 1996, Falcke, Wilson, & Simpson 1998). This seems not to be the case for NGC 4151.

In conflict with this statement, the study of NGC 4151 by Winge *et al.* (1998) reports that high velocity clouds are seen around the edges of the radio knots. This is not confirmed by Kaiser *et al.* (1999) who conclude that there is no direct association between non-virial gas kinematics, as determined by high velocity and high velocity dispersion, and proximity to the radio knots. Our results concur with those of Kaiser *et al.* (1999). While we do find high velocity clouds in our aperture there is no distinct preference for them to be found along P.A. 70° , which is more closely aligned with the radio axis (P.A. 77°).

Further support for radial outflow comes from the emission line ratios as a function of position. For example there is no significant difference in the [OIII]/[OII] or [OIII] $\lambda 5007 / H\beta$ ratios between the two slit positions even though the spectra at P.A. 70° are much more closely aligned with the radio axis than the clouds at P.A. 221° . This is in contrast to the case of NGC 1068 where the [OIII]/[OII] ratio increases dramatically in regions that coincide with the radio jet (Axon *et al.* 1998). WFPC2 images of NGC 1068 presented by Capetti, Axon, & Macchetto (1997) may also indicate higher density and ionization state along

the radio jet in this object. Furthermore, these authors suggest that an additional source of local ionizing continuum is required to explain the observations. While these results certainly raise an interesting possibility for NGC 1068, our results for NGC 4151 show no such association between the radio morphology and the emission line ratios. Thus the radio jet in NGC 4151 seems to have little influence on the ionization state of the gas. Similar results are seen for the [SII] ratio and the [OIII] $\lambda 5007 / \lambda 4363$ ratio suggesting no strong changes in the physical condition of the gas with proximity to the radio emission.

Because the line ratio diagrams show no evidence for shock or shock plus precursor ionization models at least for low velocity shocks, they support the arguments for radial outflow. If the gas were expanding away from the radio axis one would expect to see large amounts of shocked material particularly at the interface of the flow with the ambient interstellar medium of the host galaxy disk. In the case of radial outflow, we would expect to see little shocked gas since the motion is not directed into the disk and the relative velocities of gas within the flow should be small.

Perhaps an important consideration is that the radio morphology of NGC 4151 is rather different from that of Mrk 3 for example. Pedlar *et al.* have compared the radio structure of NGC 4151 to that of an FR I type radio galaxy, with much of the radio emission coming from a diffuse component, although on much smaller scales. The radio emission in Mrk 3, by contrast, is more jet-like being unresolved with MERLIN perpendicular to the radio source axis (Kukula *et al.* 1993). Thus we might consider that the radio emission in NGC 4151 is not a well collimated jet, but rather a broad spray of plasma. Gas clouds in the vicinity of the radio flow would thus be more naturally accelerated in directions roughly aligned with the radio axis than perpendicular to it.

One possible scenario is that the core of the radio jet in NGC 4151 has cleared a channel in the line emitting gas and has blown out of the disk of the galaxy as suggested by Schulz (1988). Thus there may have been a bow shock associated with the radio lobes in the past but the jet has passed on to lower density region in the outer bulge and galaxy halo. The line emitting gas is now free to flow out along the radio axis but only weakly

interacts with the jet itself and the host galaxy ISM.

NGC 4151 is also known to have a system of nuclear absorption lines, particularly CIV $\lambda 1549$, which are blueshifted with respect to the systemic velocity by values ranging from 0 to 1600 km s⁻¹ (*e.g.* Weymann *et al.* 1997). It is tempting to link the outflow seen in our study with that for the absorption line system. However, these flows are observed on vastly different scales and thus a true connection has not been established. Models invoking winds from the nucleus to explain the NLR kinematics and other properties of Seyfert galaxies have been proposed (*e.g.* Krolik & Vrtilik, 1984, Schiano, 1986, Smith, 1993). One suggestion is that X-ray heating of the molecular torus is the source of the wind (Krolik & Begelman, 1986). The base of the wind forms the electron scattering region which serves as the “mirror” allowing a view of the BLR in polarized light in some Seyfert 2 galaxies. At larger radii one might expect that the steep potential of the galaxy bulge tends to decelerate the wind. We conclude that the kinematics in NGC 4151 seem to be consistent with wind models for the NLR.

5. Summary

The results presented in this paper provide an interesting contrast to the recent work on the NLR of Seyfert galaxies. Our analysis of the longslit spectra of NGC 4151 has revealed a rather different picture of the NLR in the sense that the prominent radio jet has very little influence on the kinematics and physical conditions. We find that the kinematics are best characterized by a decelerating radial outflow from the nucleus in the form of a wind. The lack of evidence for strong shocks near the radio axis and the uniformity of the line ratios across the NLR supports this picture. Thus it appears that while interaction between the radio jet and the NLR gas may be a common occurrence it is by no means ubiquitous and does not apply in the case of NGC 4151.

We would like to thank Diane Eggers for her assistance in the data analysis. We would also like to thank Mark Allen for providing the model grids for the UV line ratio diagrams. This research has been supported in part by NASA under contract NAS5-31231.

REFERENCES

- Allen, M., Dopita, M. A., & Tsvetanov, Z. I. 1998, *ApJ*, 493, 571
- Antonucci, R., 199 *ARA&A*, 31, 473A
- Baum, S., Bohlin, R., Christensen, J., Debes. J., Downes, R., Ferguson, H., Gonnella, A., Goudfrooij, P., Hayes, J., Hodge, P., Hulbert, S., Katsanis, R., Keys, T., Lanning, H., McGrath, M., Sahu, K., Shaw, R., Smith, E., Walborn, N., Wilson, J. & Bowers, C. 1998 *STIS Instrument Handbook, Version 2.0* (Baltimore: STScI)
- Bevington, P. R. 1968, 'Data Reduction and Error Analysis for the Physical Sciences' (New York: McGraw-Hill)
- Bicknell, G. V., Dopita, M. A., Tsvetanov, Z. I., & Sutherland, R. S. 1998, *ApJ*, 495, 680
- Boksenberg, A., Catchpole, R. M., Macchetto, F., Albrecht, R., Barbieri, C., Blades, J. C., Crane, P., Deharveng, J. M., Disney, M. J., Jakobsen, P., Kampermann, T. M., King, I. R., Mackay, C. D., Paresce, F., Weigelt, G., Baxter, D., Greenfield, P., Jedrzejewski, R., Nota, A., & Sparks, W. B. 1995, *ApJ*, 440, 151
- Bosma, A. Ekers, R. D., & Lequeux, J. 1977, *A&A*, 57, 97
- Bowers, C. & Baum, S. 1998 *STIS ISR 98-24* “Spectroscopic Mode Peculiarities”
- Capetti, A., Axon, D. J., Macchetto, F. D., Marconi, A., Winge, C. 1999, *ApJ*, 516, 184
- Capetti, A., Axon, D. J., & Macchetto, F. D. 1997 *ApJ*, 487, 560
- Capetti, A., Axon, D. J., Macchetto, F., Sparks, W. B., & Boksenberg, A. 1996, *ApJ*, 469, 554
- Crenshaw, D.M., Rodriguez-Pascual, P.M., Penton, S.V., Edelson, R.A., Alloin D., et al., 1996, *ApJ*, 470, 332
- Crenshaw, D.M., & Peterson, B.M. 1986, *PASP*, 98, 185
- Evans, I. N., Ford, H. C., Kinney, A. L., Antonucci, R. R. J., Armus, L., & Caganoff, S. 1991, *ApJL*, 369, L27

- Evans, I. N., Tsvetanov, Z., Kriss, G. A., Ford, H. C., Caganoff, S., & Koratkar, A. P. 1993, *ApJ*, 417, 82
- Falcke, H., Wilson, A. S., & Simpson, C. 1998, *ApJ*, 502, 199
- Ferland, G. & Netzer, H. 1983, *ApJ*, 264, 105
- Hutchings, J.B., Crenshaw, D.M., Kaiser, M.E., Kraemer, S.B., Weistrop, D., Baum, S., Bowers, C.B., Feinberg, L. D., Green, R.F., Gull, T.R., Hartig, G.F., Hill, G., Lindler, D.J., 1998, *ApJ*, 492, L115
- Hutchings, J.B., Crenshaw, D.M., Danks, A. C., Gull, T.R., Kraemer, S.B., Nelson, C. H., Weistrop, D., Kaiser, M.E., Joseph, C. L. 1999, *AJ*, submitted
- Kaiser M.E., Bradley II, L. D., Hutchings J.B., Crenshaw, D. M., Gull, T. R., Kraemer, S. B., Nelson, C. H., Ruiz, J., & Weistrop, D. 1999, *ApJ*, in press
- Kaspi, S., Maoz, D., Netzer, H., Peterson, B.M., Alexander, T., Barth, A.J., *et al.*, 1996, *ApJ*, 470, 336
- Kimble, R.A., Woodgate, B.E., Bowers, C.W., Kraemer, S.B., Kaiser, M.E., *et al.* 1998, *ApJ*, 492, L83
- Kraemer, S. B., Crenshaw, D. M., Hutchings, J. B., Gull, T. R., Kaiser, M. E. Nelson, C. H., & Weistrop, D. M. 1999, *ApJ*, submitted (Paper II)
- Krolik, J. H. & Vrtilik, J. M. 1984, *ApJ*, 279, 521
- Krolik, J. H., & Begelman, M. C. 1986, *ApJ*, 308, L55
- Kukula, M. J., Ghosh, T., Pedlar, A., Schilizzi, R. T., Miley, G. K., de Bruyn, A. G., & Saika, D. J. 1993, *MNRAS*, 264, 893
- Lindler, D. 1998, *CALSTIS Reference Guide (CALSTIS Version 5.1)*
- Lindler, D. 1998, Private communication
- Osterbrock, D. E. 1974, *Astrophysics of Gaseous Nebulae* (San Fransisco: W. H. Freeman)
- Pedlar A., Kukula, M.J., Longley, D.P.T., Muxlow, T.W.B., Axon, D.J., Baum, S., O’Dea, C., Unger, & S.W. 1993, *MNRAS*, 263, 471
- Penston, M.V., Robinson, A., *et al.*, 1990, *AA*, 236, 53
- Peterson, B.M., Wanders, I., Bertram, R., Hunley, J.F., Pogge, R.W., Wagner, R.M., 1998, *ApJ*, 501, 82
- Robinson, A., Vila-Vilaro, B., Axon, D.J., Perez, E., Wagner, S.J., *et al.*, 1994, *AA*, 291, 351
- Schiano, A. V. R. 1986, *ApJ*, 302, 95
- Schmitt, H. R., & Kinney, A. L. 1996, *ApJ*, 463, 498
- Schulz, H. R. 1988, *A&A*, 203, 233
- Schulz, H. R. 1990, *AJ*, 99, 1442
- Shaw, R.A., & Dufour, R. J. 1995, *PASP*, 895, 107
- Simkin, S. 1975, *ApJ*, 200, 567
- Smith, S. J. 1993, *ApJ*, 411, 1993
- Sutherland, R. S., Bicknell, G. V., & Dopita, M. A. 1993, *ApJ* 414, 510
- Taylor, D., Dyson, J. E. & Axon D. E. 1992, *MNRAS*, 255, 351
- Veilleux, S. & Osterbrock, D. E. 1987, *ApJS*, 63, 295
- Ulrich, M.H., Maraschi, L., Urry, C.M., 1997, *ARAA*, 35, 445
- Warwick, R.S., Smith, D.A., Yaqoob, T., Edelson, R., Johnson, W.N., Reichert, G.A., Clavel, J., Magdziarz, P., Peterson, B.M., Zdziarski, A.A., 1996, *ApJ*, 470, 349
- Weymann, R.J., Morris, S.L., Gray, M.E., Hutchings, J.B., 1997, *ApJ*, 483, 717
- Winge C., Axon D.J., Macchetto F.D., Capetti A., & Marconi A. 1999, *ApJ*, 519, 134
- Woodgate, B.E., Kimble, R.A., Bowers, C.W., Kraemer, S., Kaiser, M.E., *et al.* 1998, *PASP*, 110, 1183

This 2-column preprint was prepared with the AAS L^AT_EX macros v5.0.

TABLE 1
STIS Longslit Observations of NGC 4151

Dataset	Date	Grating	Dispersion Å/pixel	Spectral Range	PA (°)	Ex. T. (sec)
o42302070	Feb. 10, 1998	G430L	2.73	2900–5700	221	720
o42302080	Feb. 10, 1998	G750L	4.92	5240–10270	221	720
o42302090	Feb. 10, 1998	G140L	0.6	1150–1730	221	2250
o423020a0	Feb. 10, 1998	G140L	0.6	1150–1730	221	2250
o42303050	Jan. 8, 1998	G430L	2.73	2900–5700	221	720
o42303060	Jan. 8, 1998	G750L	4.92	5240–10270	221	720
o42303070	Jan. 8, 1998	G230LB	1.35	1680–3060	221	2160
o42304090	June 1, 1998	G430L	2.73	2900–5700	70	720
o423040a0	June 1, 1998	G750L	4.92	5240–10270	70	720
o423040b0*	Jun. 1, 1998	G140L	0.6	1150–1730	70	2250
o423040c0*	Jun. 1, 1998	G140L	0.6	1150–1730	70	2250
o42305050	May 7, 1998	G430L	2.73	2900–5700	70	720
o42305060	May 7, 1998	G750L	4.92	5240–10270	70	720
o42305070	May 7, 1998	G230LB	1.35	1680–3060	70	2160

* Observations failed.

Table 2a
Observed Narrow Line Ratios Along Slit at P.A. 221° (SW side)

	0''10 – 0''30	0''30 – 0''50	0''50 – 0''70	0''70 – 0''90	0''90 – 1''10	1''50 – 1''90	1''90 – 2''30	2''30 – 2''70	2''70 – 3''30
Ly α λ 1216	5.71 (0.26)	3.54 (0.36)	2.78 (0.23)	1.93 (0.17)	0.62 (0.07)	2.08 (0.21)	2.00 (0.15)	2.07 (0.28)	—
NV λ 1240	1.22 (0.09)	0.80 (0.20)	0.63 (0.17)	0.51 (0.10)	0.21 (0.04)	0.51 (0.12)	0.39 (0.06)	0.54 (0.09)	—
CII λ 1334	0.22 (0.05)	—	0.11 (0.05)	—	0.03 (0.01)	0.09 (0.04)	0.12 (0.03)	0.15 (0.04)	—
SiIV, OIV λ 1402	1.02 (0.14)	0.59 (0.12)	0.44 (0.10)	0.25 (0.07)	0.21 (0.05)	0.41 (0.08)	0.32 (0.05)	0.51 (0.08)	—
NIV λ 1486	—	—	0.11 (0.06)	0.12 (0.06)	0.07 (0.03)	—	0.12 (0.03)	—	—
CIV λ 1550	6.64 (0.36)	2.70 (0.31)	3.05 (0.27)	1.84 (0.18)	0.72 (0.09)	1.84 (0.20)	1.63 (0.14)	2.15 (0.27)	—
HeII λ 1640	1.52 (0.19)	0.95 (0.23)	0.90 (0.16)	0.52 (0.13)	0.63 (0.08)	0.78 (0.12)	0.69 (0.09)	1.03 (0.16)	—
OIII λ 1663	0.32 (0.12)	—	—	—	—	—	0.11 (0.06)	0.21 (0.09)	—
CIII], SiIII λ 1909	2.68 (0.37)	2.98 (0.64)	1.23 (0.39)	1.87 (0.68)	1.50 (0.38)	—	—	—	—
CII], O[III] λ 2326	0.36 (0.08)	0.74 (0.12)	0.57 (0.09)	0.67 (0.14)	0.30 (0.07)	0.66 (0.28)	0.56 (0.16)	—	—
[NeIV] λ 2423	1.22 (0.10)	0.65 (0.10)	0.59 (0.10)	0.56 (0.13)	0.45 (0.07)	0.56 (0.25)	0.34 (0.16)	—	—
[OII] λ 2470	0.36 (0.08)	0.16 (0.08)	—	—	—	—	—	—	—
MgII λ 2800	0.96 (0.25)	0.65 (0.12)	0.66 (0.11)	0.69 (0.13)	0.18 (0.06)	0.85 (0.22)	0.70 (0.17)	—	—
OIII λ 3133	0.65 (0.15)	0.46 (0.19)	—	—	—	—	—	—	—
[NeV] λ 3346	0.36 (0.06)	0.24 (0.11)	0.28 (0.14)	0.26 (0.13)	0.18 (0.08)	—	—	—	0.97 (1.27)
[NeV] λ 3426	1.01 (0.08)	0.70 (0.14)	0.98 (0.14)	0.63 (0.14)	0.51 (0.12)	—	—	—	0.99 (1.82)
[FeVII] λ 3588	0.14 (0.06)	—	—	—	—	—	—	—	—
[OII] λ 3727	1.31 (0.13)	1.87 (0.24)	1.98 (0.16)	2.37 (0.15)	1.78 (0.16)	3.27 (0.31)	3.14 (0.25)	3.15 (0.40)	4.59 (2.08)
[FeVII] λ 3760	0.28 (0.06)	—	—	—	—	—	—	—	—
[NeIII] λ 3869	1.68 (0.08)	1.46 (0.14)	1.27 (0.11)	1.06 (0.09)	1.04 (0.08)	1.15 (0.15)	0.90 (0.10)	0.80 (0.17)	1.81 (1.00)
H ζ , HeI λ 3889	0.36 (0.05)	0.28 (0.06)	0.18 (0.06)	0.12 (0.05)	0.15 (0.04)	0.20 (0.09)	0.17 (0.07)	0.37 (0.19)	—
[NeIII], He λ 3967	0.66 (0.05)	0.55 (0.10)	0.52 (0.07)	0.44 (0.06)	0.46 (0.05)	0.42 (0.10)	0.48 (0.07)	0.47 (0.13)	—
[SII] λ 4072	0.38 (0.05)	0.29 (0.07)	0.23 (0.05)	0.28 (0.05)	0.23 (0.05)	0.21 (0.07)	0.28 (0.07)	—	—
H δ λ 4100	0.43 (0.05)	0.32 (0.06)	0.31 (0.08)	0.26 (0.06)	0.36 (0.05)	0.23 (0.08)	0.30 (0.06)	0.49 (0.13)	0.21 (0.37)
H γ λ 4340	0.64 (0.05)	0.42 (0.06)	0.59 (0.07)	0.44 (0.05)	0.47 (0.04)	0.63 (0.12)	0.46 (0.06)	0.43 (0.13)	0.56 (0.43)
[OIII] λ 4363	0.34 (0.05)	0.22 (0.05)	0.29 (0.05)	0.16 (0.04)	0.30 (0.04)	0.23 (0.06)	0.19 (0.05)	0.20 (0.10)	0.12 (0.24)
HeII λ 4686	0.31 (0.04)	0.33 (0.06)	0.23 (0.04)	0.24 (0.04)	0.23 (0.03)	0.11 (0.06)	0.23 (0.05)	0.20 (0.10)	0.21 (0.33)
H β λ 4861	1.00 (0.00)	1.00 (0.00)	1.00 (0.00)	1.00 (0.00)	1.00 (0.00)	1.00 (0.00)	1.00 (0.00)	1.00 (0.00)	1.00 (0.49)
[OIII] λ 4959	5.38 (0.29)	4.62 (0.37)	4.22 (0.25)	3.57 (0.20)	4.41 (0.25)	3.76 (0.32)	2.66 (0.17)	2.86 (0.32)	3.04 (1.19)
[OIII] λ 5007	16.05 (0.65)	14.00 (1.08)	12.94 (0.82)	11.18 (0.58)	13.32 (0.71)	11.25 (0.90)	7.82 (0.47)	8.62 (0.90)	5.96 (2.49)
[NI] λ 5200	—	—	0.09 (0.04)	0.10 (0.03)	0.05 (0.02)	0.12 (0.05)	—	—	—
[FeVII] λ 5721	0.14 (0.03)	—	—	—	—	—	—	—	—
[NII] λ 5755	—	—	—	—	0.06 (0.03)	—	—	—	—
HeI λ 5876	0.24 (0.05)	0.14 (0.06)	0.14 (0.05)	0.12 (0.06)	0.13 (0.04)	—	—	0.29 (0.14)	—
[FeVII] λ 6087	0.36 (0.05)	0.11 (0.07)	0.13 (0.05)	—	—	—	—	—	—
[OI] λ 6300	0.95 (0.06)	0.92 (0.09)	0.94 (0.10)	0.70 (0.06)	0.46 (0.04)	0.63 (0.09)	0.61 (0.07)	0.45 (0.10)	—
[OI] λ 6364	0.46 (0.05)	0.15 (0.04)	0.22 (0.05)	0.14 (0.03)	0.17 (0.03)	0.21 (0.07)	0.21 (0.05)	0.15 (0.12)	—
[NII] λ 6548	0.80 (0.27)	1.04 (0.14)	0.73 (0.09)	0.74 (0.15)	0.62 (0.06)	0.94 (0.16)	0.86 (0.11)	0.94 (0.15)	—
H α λ 6563	4.01 (0.82)	3.36 (0.51)	3.04 (0.37)	3.13 (0.58)	3.49 (0.28)	3.37 (0.52)	2.97 (0.36)	3.19 (0.54)	—
[NII] λ 6584	2.41 (0.81)	3.13 (0.40)	2.20 (0.29)	2.23 (0.46)	1.86 (0.17)	2.81 (0.50)	2.58 (0.35)	2.84 (0.45)	—
[SII] λ 6717	0.46 (0.03)	0.36 (0.05)	0.64 (0.06)	0.71 (0.06)	0.47 (0.04)	0.72 (0.10)	0.99 (0.08)	0.95 (0.14)	—
[SII] λ 6731	0.67 (0.05)	0.60 (0.08)	0.72 (0.07)	0.86 (0.08)	0.60 (0.05)	1.01 (0.14)	0.98 (0.08)	0.82 (0.12)	—
[SII] $\lambda\lambda$ 6716, 6731	1.13 (0.06)	0.96 (0.09)	1.36 (0.09)	1.57 (0.10)	1.07 (0.06)	1.73 (0.17)	1.97 (0.11)	1.77 (0.18)	—
ArIII λ 7136	0.21 (0.03)	0.32 (0.08)	0.26 (0.05)	0.35 (0.05)	0.28 (0.04)	0.21 (0.06)	0.19 (0.05)	0.21 (0.09)	—
[OII] λ 7325	0.31 (0.04)	0.26 (0.06)	0.24 (0.05)	0.21 (0.04)	0.18 (0.03)	0.17 (0.06)	0.23 (0.06)	0.22 (0.11)	—
[SIII] λ 9069	0.89 (0.21)	0.43 (0.07)	0.52 (0.07)	0.51 (0.07)	0.40 (0.05)	0.44 (0.09)	0.29 (0.08)	0.50 (0.18)	—
[SIII] λ 9532	2.14 (0.33)	1.56 (0.14)	1.44 (0.15)	1.62 (0.13)	1.33 (0.08)	1.63 (0.18)	1.06 (0.13)	1.07 (0.26)	—
F(H β) λ 4861)	9.76 (0.37)	4.31 (0.33)	3.65 (0.21)	2.35 (0.11)	4.52 (0.24)	1.90 (0.15)	2.35 (0.14)	1.07 (0.11)	0.31 (0.11)

Table 2b
Observed Narrow Line Ratios Along Slit at P.A. 221° (NE side)

	0''10 – 0''30	0''30 – 0''50	0''50 – 0''70	0''70 – 0''90	0''90 – 1''10	1''50 – 1''90	1''90 – 2''30	2''30 – 2''70	2''70 – 3''10	3''10 – 3''50
Ly α λ 1216	2.64 (0.25)	6.17 (0.39)	12.30 (1.16)	11.49 (0.88)	7.57 (0.60)	7.83 (1.53)	6.20 (0.87)	5.35 (0.82)	—	—
NV λ 1240	1.00 (0.24)	0.40 (0.09)	0.35 (0.14)	0.30 (0.07)	0.24 (0.04)	0.68 (0.20)	0.46 (0.13)	0.33 (0.09)	—	—
CII λ 1334	0.26 (0.09)	—	—	0.14 (0.04)	0.09 (0.02)	0.21 (0.12)	—	—	—	—
SiIV, OIV] λ 1402	0.57 (0.17)	0.43 (0.13)	0.67 (0.22)	0.34 (0.09)	0.27 (0.05)	0.64 (0.21)	0.32 (0.10)	0.22 (0.12)	—	—
NIV] λ 1486	—	0.22 (0.09)	—	—	—	—	—	—	—	—
CIV λ 1550	2.94 (0.33)	2.66 (0.24)	3.31 (0.48)	2.19 (0.24)	2.37 (0.20)	3.13 (0.65)	2.92 (0.43)	2.70 (0.43)	—	—
HeII λ 1640	0.60 (0.21)	1.31 (0.17)	1.07 (0.26)	1.01 (0.14)	0.96 (0.12)	1.30 (0.33)	0.88 (0.20)	0.97 (0.18)	—	—
OIII] λ 1663	—	0.21 (0.10)	—	0.17 (0.09)	0.17 (0.06)	—	—	—	—	—
CIII], SiIII] λ 1909	1.18 (0.37)	1.95 (0.41)	2.43 (1.03)	1.54 (0.47)	2.44 (0.78)	—	—	—	—	—
CII], O[III] λ 2326	0.37 (0.11)	0.52 (0.08)	0.75 (0.20)	1.05 (0.19)	0.71 (0.11)	—	—	—	—	—
[NeIV] λ 2423	0.37 (0.08)	0.65 (0.08)	0.45 (0.17)	0.38 (0.09)	0.32 (0.11)	—	—	—	—	—
[OII] λ 2470	—	0.18 (0.08)	—	0.29 (0.11)	0.16 (0.08)	—	—	—	—	—
MgII λ 2800	0.47 (0.29)	0.50 (0.07)	0.61 (0.18)	1.48 (0.16)	0.88 (0.13)	—	—	—	—	—
OIII λ 3133	—	0.46 (0.16)	—	—	—	—	—	—	1.99 (2.69)	1.71 (5.68)
[NeV] λ 3346	—	0.28 (0.12)	—	—	—	—	—	—	1.06 (1.58)	—
[NeV] λ 3426	0.68 (0.12)	0.65 (0.13)	0.38 (0.18)	0.71 (0.19)	0.47 (0.19)	—	—	—	—	4.27 (3.11)
[FeVII] λ 3588	—	—	—	—	—	—	—	—	—	—
[OII] λ 3727	1.46 (0.13)	1.72 (0.14)	2.12 (0.25)	2.73 (0.25)	2.62 (0.20)	4.70 (1.00)	3.82 (0.60)	4.62 (0.76)	4.43 (4.09)	3.87 (2.69)
[FeVII] λ 3760	0.22 (0.08)	—	—	—	—	—	—	—	—	—
[NeIII] λ 3869	1.13 (0.10)	1.42 (0.11)	1.44 (0.17)	1.42 (0.14)	1.17 (0.12)	1.21 (0.41)	1.24 (0.25)	1.54 (0.33)	1.10 (1.33)	2.52 (1.93)
H ζ , HeI λ 3889	0.16 (0.06)	0.26 (0.06)	0.33 (0.09)	0.21 (0.06)	0.19 (0.07)	—	—	—	—	1.59 (1.51)
[NeIII], He λ 3967	0.49 (0.06)	0.58 (0.06)	0.65 (0.11)	0.69 (0.08)	0.54 (0.08)	1.00 (0.37)	0.70 (0.25)	0.64 (0.24)	—	—
[SII] λ 4072	0.29 (0.06)	0.26 (0.06)	0.48 (0.10)	0.53 (0.08)	0.29 (0.06)	—	—	—	—	1.37 (3.10)
H δ λ 4100	0.22 (0.05)	0.26 (0.05)	0.33 (0.08)	0.40 (0.10)	0.24 (0.06)	—	0.36 (0.18)	0.52 (0.23)	—	—
H γ λ 4340	0.36 (0.05)	0.56 (0.06)	0.52 (0.09)	0.65 (0.08)	0.49 (0.06)	—	0.61 (0.18)	0.65 (0.28)	0.28 (0.51)	—
[OIII] λ 4363	0.26 (0.05)	0.29 (0.05)	0.29 (0.08)	0.44 (0.07)	0.21 (0.05)	—	0.29 (0.15)	—	0.44 (1.10)	1.27 (2.54)
HeII λ 4686	0.32 (0.05)	0.20 (0.04)	0.25 (0.07)	0.22 (0.05)	0.17 (0.04)	0.42 (0.20)	0.26 (0.14)	0.36 (0.18)	—	1.00 (2.17)
H β λ 4861	1.00 (0.00)	1.00 (0.00)	1.00 (0.00)	1.00 (0.00)	1.00 (0.00)	1.00 (0.00)	1.00 (0.00)	1.00 (0.00)	1.00 (1.17)	1.00 (0.79)
[OIII] λ 4959	4.35 (0.27)	4.67 (0.28)	4.71 (0.45)	4.14 (0.33)	3.56 (0.26)	4.11 (0.81)	4.08 (0.56)	3.80 (0.57)	1.91 (1.75)	3.61 (2.18)
[OIII] λ 5007	13.26 (0.80)	14.18 (0.82)	14.30 (1.29)	12.42 (0.95)	10.56 (0.74)	11.00 (2.09)	12.66 (1.71)	11.52 (1.68)	5.70 (5.01)	8.10 (4.62)
[NI] λ 5200	—	0.11 (0.05)	—	0.17 (0.06)	—	—	—	—	—	—
[FeVII] λ 5721	—	—	—	—	—	—	—	—	—	—
[NII] λ 5755	—	0.14 (0.05)	—	—	—	—	—	—	—	—
HeI λ 5876	0.17 (0.05)	0.17 (0.05)	—	0.20 (0.07)	0.14 (0.07)	—	—	—	—	—
[FeVII] λ 6087	—	—	—	—	—	—	—	—	—	—
[OI] λ 6300	0.80 (0.07)	0.98 (0.11)	0.71 (0.09)	1.06 (0.14)	0.62 (0.07)	0.87 (0.26)	0.53 (0.17)	0.52 (0.19)	—	—
[OI] λ 6364	0.24 (0.04)	0.31 (0.07)	0.15 (0.06)	0.32 (0.06)	0.21 (0.05)	—	—	—	—	—
[NII] λ 6548	0.80 (0.18)	0.75 (0.10)	0.71 (0.13)	0.95 (0.13)	0.89 (0.11)	1.17 (0.29)	0.84 (0.17)	0.84 (0.17)	—	—
H α λ 6563	3.98 (0.70)	3.79 (0.49)	2.86 (0.50)	3.23 (0.45)	3.06 (0.47)	4.17 (0.96)	3.29 (0.66)	3.00 (0.64)	—	—
[NII] λ 6584	2.39 (0.55)	2.24 (0.30)	2.15 (0.41)	2.85 (0.39)	2.66 (0.35)	3.53 (0.79)	2.53 (0.51)	2.54 (0.51)	—	—
[SII] λ 6717	0.46 (0.07)	0.64 (0.09)	0.73 (0.10)	0.75 (0.09)	0.51 (0.05)	0.72 (0.23)	0.87 (0.16)	0.88 (0.18)	—	—
[SII] λ 6731	0.64 (0.10)	0.86 (0.12)	0.77 (0.11)	0.71 (0.08)	0.76 (0.08)	0.83 (0.26)	0.70 (0.14)	0.71 (0.14)	—	—
[SII] λ λ 6716, 6731	1.10 (0.12)	1.50 (0.15)	1.50 (0.15)	1.46 (0.12)	1.27 (0.09)	1.55 (0.35)	1.57 (0.21)	1.59 (0.23)	—	—
ArIII λ 7136	0.21 (0.05)	0.26 (0.04)	0.29 (0.07)	0.42 (0.08)	0.14 (0.05)	0.51 (0.26)	0.29 (0.14)	—	—	—
[OII] λ 7325	0.23 (0.03)	0.30 (0.04)	0.32 (0.07)	0.58 (0.09)	0.23 (0.06)	—	—	—	—	—
[SIII] λ 9069	0.98 (0.09)	0.50 (0.05)	0.73 (0.14)	0.70 (0.12)	0.47 (0.07)	—	0.54 (0.22)	0.58 (0.23)	—	—
[SIII] λ 9532	2.65 (0.18)	1.30 (0.09)	1.78 (0.27)	1.31 (0.14)	1.00 (0.17)	—	1.08 (0.33)	1.38 (0.38)	—	—
F(H β λ 4861)	6.18 (0.37)	5.07 (0.29)	1.78 (0.16)	3.21 (0.24)	3.31 (0.21)	0.53 (0.10)	0.76 (0.10)	0.69 (0.10)	0.18 (0.14)	0.13 (0.08)

Table 2c
Observed Narrow Line Ratios Along Slit at P.A. 70° (SW side)

	0''.10 – 0''.30	0''.30 – 0''.50	0''.50 – 0''.70	0''.70 – 0''.90	0''.90 – 1''.10	1''.10 – 1''.55	1''.55 – 2''.00	2''.00 – 2''.40	2''.70 – 3''.10
CIII], SiIII]λ1909	1.66 (0.28)	2.72 (0.43)	1.97 (0.29)	1.28 (0.26)	1.67 (0.27)	1.31 (0.21)	–	–	–
CII], O[III]λ2326	0.62 (0.08)	0.63 (0.09)	0.73 (0.06)	0.49 (0.06)	0.51 (0.06)	0.34 (0.04)	–	–	–
[NeIV]λ2423	0.57 (0.07)	0.27 (0.07)	0.36 (0.06)	0.39 (0.05)	0.36 (0.05)	0.39 (0.04)	–	–	–
[OII]λ2470	0.08 (0.05)	0.26 (0.06)	0.32 (0.05)	0.12 (0.04)	0.15 (0.04)	0.15 (0.04)	–	–	–
MgIIλ2800	0.89 (0.10)	0.44 (0.10)	0.56 (0.05)	0.39 (0.05)	0.47 (0.05)	0.36 (0.04)	–	–	–
OIIIλ3133	0.18 (0.06)	0.26 (0.09)	0.17 (0.06)	0.10 (0.05)	0.24 (0.06)	0.11 (0.04)	0.55 (0.17)	1.56 (1.24)	4.82 (2.51)
[NeV]λ3346	0.44 (0.07)	0.16 (0.05)	0.16 (0.04)	0.18 (0.04)	0.14 (0.04)	0.09 (0.02)	0.23 (0.11)	2.00 (0.79)	1.51 (0.96)
[NeV]λ3426	0.90 (0.06)	0.42 (0.07)	0.34 (0.05)	0.56 (0.06)	0.28 (0.04)	0.29 (0.03)	0.59 (0.15)	0.97 (0.50)	0.95 (0.36)
[FeVII]λ3588	0.06 (0.02)	0.04 (0.03)	0.09 (0.03)	0.03 (0.02)	0.06 (0.03)	0.03 (0.02)	0.16 (0.08)	1.08 (0.70)	0.55 (0.20)
[OII]λ3727	1.17 (0.06)	1.71 (0.09)	2.36 (0.07)	2.01 (0.07)	2.75 (0.09)	2.47 (0.06)	2.69 (0.22)	3.22 (0.99)	3.31 (0.66)
[FeVII]λ3760	–	–	–	–	–	–	–	–	–
[NeIII]λ3869	1.13 (0.05)	1.24 (0.06)	1.15 (0.04)	1.10 (0.04)	1.08 (0.04)	1.07 (0.03)	0.77 (0.09)	1.32 (0.41)	0.77 (0.22)
Hζ, HeIλ3889	0.17 (0.03)	0.07 (0.02)	0.17 (0.02)	0.14 (0.02)	0.17 (0.02)	0.19 (0.02)	0.15 (0.06)	0.59 (0.22)	0.31 (0.17)
[NeIII], Heλ3967	0.51 (0.03)	0.54 (0.04)	0.53 (0.03)	0.47 (0.03)	0.50 (0.02)	0.50 (0.02)	0.34 (0.07)	0.74 (0.27)	0.21 (0.11)
[SII]λ4072	0.31 (0.03)	0.42 (0.04)	0.44 (0.02)	0.25 (0.02)	0.27 (0.02)	0.25 (0.02)	0.20 (0.07)	0.26 (0.16)	0.44 (0.16)
Hδλ4100	0.19 (0.02)	0.17 (0.02)	0.19 (0.02)	0.23 (0.02)	0.21 (0.02)	0.22 (0.01)	0.19 (0.06)	0.21 (0.19)	0.22 (0.15)
Hγλ4340	0.47 (0.03)	0.41 (0.03)	0.42 (0.02)	0.49 (0.03)	0.45 (0.02)	0.47 (0.02)	0.22 (0.06)	0.79 (0.43)	0.64 (0.18)
[OIII]λ4363	0.27 (0.02)	0.16 (0.02)	0.12 (0.02)	0.21 (0.02)	0.16 (0.02)	0.20 (0.01)	0.12 (0.05)	0.30 (0.20)	0.46 (0.17)
HeIIλ4686	0.27 (0.02)	0.24 (0.03)	0.16 (0.02)	0.19 (0.02)	0.18 (0.01)	0.24 (0.01)	0.23 (0.05)	0.33 (0.19)	0.55 (0.17)
Hβλ4861	1.00 (0.04)	1.00 (0.05)	1.00 (0.03)	1.00 (0.03)	1.00 (0.03)	1.00 (0.02)	1.00 (0.09)	1.00 (0.35)	1.00 (0.23)
[OIII]λ4959	4.84 (0.15)	3.99 (0.15)	3.31 (0.08)	4.04 (0.10)	3.83 (0.10)	3.84 (0.07)	3.15 (0.21)	1.62 (0.47)	2.96 (0.53)
[OIII]λ5007	14.46 (0.44)	11.84 (0.42)	9.89 (0.24)	12.14 (0.30)	10.78 (0.26)	11.56 (0.21)	8.43 (0.53)	4.93 (1.30)	7.66 (1.29)
[NI]λ5200	0.03 (0.01)	0.06 (0.02)	0.10 (0.02)	0.09 (0.01)	0.10 (0.02)	0.08 (0.01)	0.13 (0.05)	0.10 (0.20)	–
[FeVII]λ5721	0.08 (0.03)	–	–	0.06 (0.03)	–	–	–	–	–
[NII]λ5755	0.05 (0.04)	–	0.08 (0.04)	0.05 (0.03)	0.04 (0.03)	0.01 (0.04)	0.08 (0.14)	–	–
HeIλ5876	0.08 (0.04)	–	0.12 (0.04)	0.14 (0.04)	0.07 (0.03)	0.06 (0.04)	0.11 (0.12)	–	–
[FeVII]λ6087	0.20 (0.04)	–	0.06 (0.03)	0.10 (0.03)	0.06 (0.03)	0.10 (0.04)	–	–	–
[OI]λ6300	0.61 (0.05)	–	0.85 (0.05)	0.69 (0.05)	0.62 (0.04)	0.79 (0.06)	0.70 (0.14)	–	0.48 (0.35)
[OI]λ6364	0.20 (0.04)	–	0.28 (0.03)	0.19 (0.03)	0.18 (0.03)	0.24 (0.04)	0.16 (0.10)	–	–
[NII]λ6548	0.70 (0.03)	0.91 (0.04)	1.09 (0.03)	0.76 (0.03)	0.81 (0.03)	0.86 (0.02)	0.84 (0.07)	0.80 (0.28)	0.63 (0.15)
Hαλ6563	3.84 (0.13)	2.85 (0.11)	3.19 (0.08)	2.95 (0.08)	3.01 (0.08)	2.92 (0.06)	2.45 (0.16)	1.71 (0.53)	2.00 (0.38)
[NII]λ6584	2.09 (0.08)	2.72 (0.11)	3.27 (0.08)	2.28 (0.07)	2.44 (0.07)	2.56 (0.05)	2.51 (0.17)	2.30 (0.69)	1.88 (0.36)
[SII]λ6717	0.32 (0.02)	0.38 (0.02)	0.72 (0.03)	0.66 (0.03)	0.64 (0.02)	0.60 (0.02)	0.68 (0.07)	0.47 (0.21)	0.58 (0.17)
[SII]λ6731	0.79 (0.03)	0.76 (0.04)	1.03 (0.03)	0.84 (0.03)	0.84 (0.03)	0.83 (0.02)	0.96 (0.09)	0.95 (0.35)	0.65 (0.18)
[SII]λλ6716, 6731	1.09 (0.05)	1.09 (0.06)	1.75 (0.05)	1.50 (0.05)	1.47 (0.04)	1.43 (0.03)	1.64 (0.13)	1.37 (0.47)	1.33 (0.31)
ArIIIλ7136	0.16 (0.04)	–	0.27 (0.03)	0.26 (0.04)	0.30 (0.03)	0.37 (0.05)	0.13 (0.10)	–	–
[OII]λ7325	0.21 (0.04)	–	0.41 (0.04)	0.26 (0.04)	0.26 (0.03)	0.35 (0.05)	0.18 (0.13)	–	–
[SIII]λ9069	0.21 (0.07)	0.45 (0.08)	0.42 (0.05)	0.40 (0.06)	0.41 (0.05)	0.36 (0.04)	0.32 (0.19)	–	–
[SIII]λ9532	0.44 (0.09)	1.18 (0.12)	0.92 (0.08)	0.85 (0.08)	0.65 (0.07)	0.75 (0.06)	0.74 (0.27)	–	–
F(Hβλ4861)	4.11 (0.12)	2.69 (0.09)	3.78 (0.09)	3.48 (0.08)	3.93 (0.09)	6.28 (0.01)	1.05 (0.00)	0.26 (0.00)	0.39 (0.01)

Table 2d
Observed Narrow Line Ratios Along Slit at P.A. 221° (NE side)

	0''.10 – 0''.30	0''.30 – 0''.50	0''.50 – 0''.75	0''.75 – 1''.00	1''.00 – 1''.20	1''.20 – 1''.55	1''.55 – 2''.05	2''.50 – 2''.90	2''.90 – 3''.50
CIII], SiIII]λ1909	2.89 (0.56)	1.74 (0.30)	2.08 (0.31)	1.88 (0.29)	1.24 (0.77)	–	–	–	–
CII], O[III]λ2326	–	0.38 (0.07)	0.34 (0.05)	0.31 (0.06)	0.49 (0.09)	0.75 (0.23)	–	–	–
[NeIV]λ2423	–	0.42 (0.05)	0.38 (0.05)	0.26 (0.06)	0.14 (0.05)	0.65 (0.21)	–	–	–
[OII]λ2470	–	0.08 (0.04)	0.15 (0.04)	0.10 (0.05)	–	–	–	–	–
MgIIλ2800	–	0.35 (0.04)	0.31 (0.05)	0.20 (0.04)	0.53 (0.06)	0.87 (0.18)	–	–	–
OIIIλ3133	0.23 (0.12)	0.26 (0.06)	0.16 (0.05)	0.11 (0.05)	0.24 (0.10)	0.21 (0.16)	0.68 (0.48)	0.75 (0.49)	1.56 (0.83)
[NeV]λ3346	0.27 (0.11)	0.29 (0.04)	0.36 (0.08)	0.21 (0.05)	0.14 (0.05)	–	0.70 (0.34)	0.54 (0.50)	1.21 (0.69)
[NeV]λ3426	0.93 (0.11)	0.72 (0.05)	0.82 (0.06)	0.37 (0.05)	0.24 (0.05)	0.39 (0.14)	1.20 (0.39)	0.64 (0.35)	1.18 (0.52)
[FeVII]λ3588	0.10 (0.05)	0.05 (0.03)	0.04 (0.02)	0.03 (0.02)	0.06 (0.03)	0.23 (0.11)	–	1.19 (0.76)	0.43 (0.30)
[OII]λ3727	1.85 (0.15)	1.70 (0.06)	1.51 (0.05)	1.74 (0.06)	2.98 (0.10)	3.94 (0.30)	3.01 (0.48)	2.93 (0.58)	3.27 (0.64)
[FeVII]λ3760	–	–	–	–	–	–	–	–	–
[NeIII]λ3869	1.25 (0.10)	1.18 (0.04)	1.21 (0.04)	1.01 (0.04)	1.02 (0.05)	1.01 (0.12)	1.04 (0.22)	0.81 (0.23)	1.41 (0.35)
Hζ, HeIλ3889	0.22 (0.05)	0.18 (0.02)	0.20 (0.02)	0.15 (0.02)	0.20 (0.03)	0.21 (0.06)	0.57 (0.18)	0.39 (0.19)	0.35 (0.20)
[NeIII], Heλ3967	0.38 (0.05)	0.51 (0.03)	0.58 (0.03)	0.41 (0.02)	0.44 (0.03)	0.40 (0.07)	0.41 (0.15)	0.57 (0.22)	0.78 (0.25)
[SII]λ4072	0.25 (0.05)	0.31 (0.03)	0.28 (0.02)	0.24 (0.02)	0.38 (0.03)	0.34 (0.07)	0.28 (0.12)	0.35 (0.14)	0.59 (0.29)
Hδλ4100	0.25 (0.04)	0.26 (0.02)	0.28 (0.02)	0.24 (0.02)	0.19 (0.02)	0.46 (0.07)	0.27 (0.24)	–	0.51 (0.31)
Hγλ4340	0.53 (0.05)	0.44 (0.02)	0.42 (0.02)	0.38 (0.02)	0.46 (0.03)	0.36 (0.06)	–	0.65 (0.19)	0.22 (0.15)
[OIII]λ4363	0.36 (0.05)	0.25 (0.02)	0.25 (0.02)	0.18 (0.02)	0.16 (0.02)	0.16 (0.06)	0.29 (0.08)	0.81 (0.20)	0.58 (0.18)
HeIIλ4686	0.29 (0.04)	0.28 (0.02)	0.27 (0.02)	0.19 (0.01)	0.20 (0.02)	0.15 (0.04)	0.20 (0.08)	1.42 (0.50)	0.54 (0.20)
Hβλ4861	1.00 (0.08)	1.00 (0.03)	1.00 (0.03)	1.00 (0.03)	1.00 (0.04)	1.00 (0.09)	1.00 (0.18)	1.00 (0.22)	1.00 (0.23)
[OIII]λ4959	5.08 (0.30)	4.14 (0.10)	4.40 (0.10)	4.08 (0.09)	3.06 (0.09)	2.77 (0.19)	2.24 (0.35)	2.30 (0.39)	2.10 (0.39)
[OIII]λ5007	14.88 (0.87)	12.84 (0.29)	13.01 (0.29)	12.29 (0.27)	9.53 (0.27)	8.07 (0.53)	7.27 (0.99)	6.99 (1.10)	6.27 (1.05)
[NI]λ5200	0.13 (0.04)	0.06 (0.01)	0.10 (0.01)	0.15 (0.01)	0.15 (0.02)	0.15 (0.05)	0.42 (0.36)	0.32 (0.15)	0.27 (0.14)
[FeVII]λ5721	0.12 (0.09)	0.05 (0.03)	0.04 (0.04)	0.05 (0.03)	0.01 (0.04)	0.27 (0.16)	–	–	–
[NII]λ5755	0.07 (0.09)	0.04 (0.03)	0.02 (0.03)	0.06 (0.04)	0.05 (0.04)	0.07 (0.11)	–	–	–
HeIλ5876	0.16 (0.09)	0.08 (0.03)	0.09 (0.04)	0.12 (0.05)	0.10 (0.05)	0.11 (0.12)	–	–	–
[FeVII]λ6087	0.20 (0.09)	0.11 (0.04)	0.10 (0.04)	0.08 (0.03)	0.10 (0.06)	0.16 (0.23)	–	–	–
[OI]λ6300	0.99 (0.12)	0.70 (0.04)	0.72 (0.05)	0.92 (0.05)	0.91 (0.06)	0.76 (0.13)	0.23 (0.26)	–	–
[OI]λ6364	0.44 (0.10)	0.21 (0.03)	0.28 (0.04)	0.35 (0.04)	0.30 (0.04)	0.28 (0.11)	0.34 (0.26)	–	–
[NII]λ6548	0.88 (0.13)	0.84 (0.04)	0.65 (0.03)	0.88 (0.04)	1.00 (0.04)	1.00 (0.08)	0.64 (0.11)	0.54 (0.11)	0.54 (0.13)
Hαλ6563	4.32 (0.37)	3.31 (0.09)	2.92 (0.09)	3.27 (0.09)	2.99 (0.10)	3.03 (0.22)	2.60 (0.36)	2.59 (0.43)	2.03 (0.38)
[NII]λ6584	2.65 (0.26)	2.52 (0.08)	1.96 (0.07)	2.63 (0.08)	2.99 (0.10)	3.00 (0.22)	1.89 (0.27)	1.63 (0.28)	1.63 (0.31)
[SII]λ6717	0.71 (0.11)	0.59 (0.03)	0.51 (0.03)	0.74 (0.03)	0.76 (0.03)	0.75 (0.09)	0.58 (0.17)	0.63 (0.17)	0.58 (0.18)
[SII]λ6731	0.84 (0.12)	0.85 (0.03)	0.68 (0.03)	0.93 (0.03)	0.99 (0.04)	0.97 (0.11)	0.57 (0.17)	0.58 (0.16)	0.29 (0.12)
[SII]λλ6716, 6731	1.54 (0.20)	1.43 (0.05)	1.19 (0.04)	1.67 (0.05)	1.75 (0.06)	1.72 (0.16)	1.16 (0.26)	1.21 (0.27)	1.26 (0.30)
ArIIIλ7136	0.22 (0.08)	0.25 (0.03)	0.20 (0.03)	0.26 (0.04)	0.26 (0.04)	0.23 (0.14)	–	–	–
[OII]λ7325	0.28 (0.10)	0.32 (0.04)	0.24 (0.04)	0.35 (0.04)	0.45 (0.05)	0.19 (0.13)	–	0.29 (0.35)	–
[SIII]λ9069	–	0.47 (0.05)	0.37 (0.06)	0.55 (0.06)	0.36 (0.07)	–	–	–	–
[SIII]λ9532	–	0.80 (0.07)	0.86 (0.08)	1.28 (0.09)	0.88 (0.10)	–	–	–	–
F(Hβλ4861)	2.13 (0.12)	3.63 (0.08)	3.87 (0.09)	3.95 (0.08)	2.71 (0.08)	1.01 (0.00)	0.52 (0.00)	0.36 (0.00)	0.39 (0.00)

Table 3a
 [OIII] λ 5007 Velocities Along P.A. 221°

Slit Pos.	Component A	Component B	Component C
-6.5	-6.3	22.29	—
-6.1	-5.9	-9.46	—
-5.9	-5.7	19.00	—
-5.7	-5.5	4.50	—
-3.1	-2.9	-281.18	—
-2.9	-2.7	-182.56	—
-2.7	-2.5	-162.13	—
-2.5	-2.3	-161.77	—
-2.3	-2.1	-145.77	—
-2.1	-1.9	-188.67	—
-1.9	-1.7	-209.34	—
-1.7	-1.5	-575.19	-131.27
-1.5	-1.3	-203.59	—
-1.3	-1.1	-293.23	43.62
-1.1	-0.9	-281.30	—
-0.9	-0.7	-898.62	-285.50
-0.7	-0.5	-834.69	-247.09
-0.5	-0.3	-754.40	-156.92
-0.3	-0.1	16.18	—
0.1	0.3	46.92	—
0.3	0.5	142.19	500.72
0.5	0.7	363.28	—
0.7	0.9	13.31	498.57
0.9	1.1	280.83	—
1.7	1.9	211.99	—
1.9	2.1	187.18	—
2.1	2.3	198.33	—
2.3	2.5	179.27	—
2.5	2.7	128.10	—
2.65	3.05	124.57	—
3.1	3.3	129.84	—

Table 3b
 [OIII] λ 5007 Velocities Along P.A. 70°

Slit Pos.	Component A	Component B	Component C
-3.1	-2.9	-130.25	—
-2.9	-2.7	-113.84	—
-2.2	-2.	-487.35	-45.29
-2.	-1.8	-176.51	—
-1.8	-1.55	-133.49	—
-1.55	-1.35	-122.94	—
-1.35	-1.1	-220.37	—
-1.1	-0.9	-1040.86	-73.93
-0.9	-0.7	-789.33	-160.39
-0.7	-0.5	-330.37	133.56
-0.5	-0.3	-872.85	-339.18
-0.3	-0.1	-313.30	147.52
0.1	0.3	99.76	668.85
0.3	0.5	45.84	504.38
0.5	0.75	58.36	—
0.75	1.	68.55	474.66
1.	1.2	114.74	—
1.2	1.4	211.21	—
1.4	1.55	203.78	—
1.55	1.8	163.10	684.91
1.8	2.05	153.45	—
2.5	2.7	192.22	—
2.7	2.9	176.16	—
2.9	3.1	187.18	—
3.1	3.3	178.91	—
3.3	3.5	167.71	—
3.5	3.8	144.53	—
4.15	4.75	130.28	—

TABLE 4a
Cloud Identification P.A. 221°

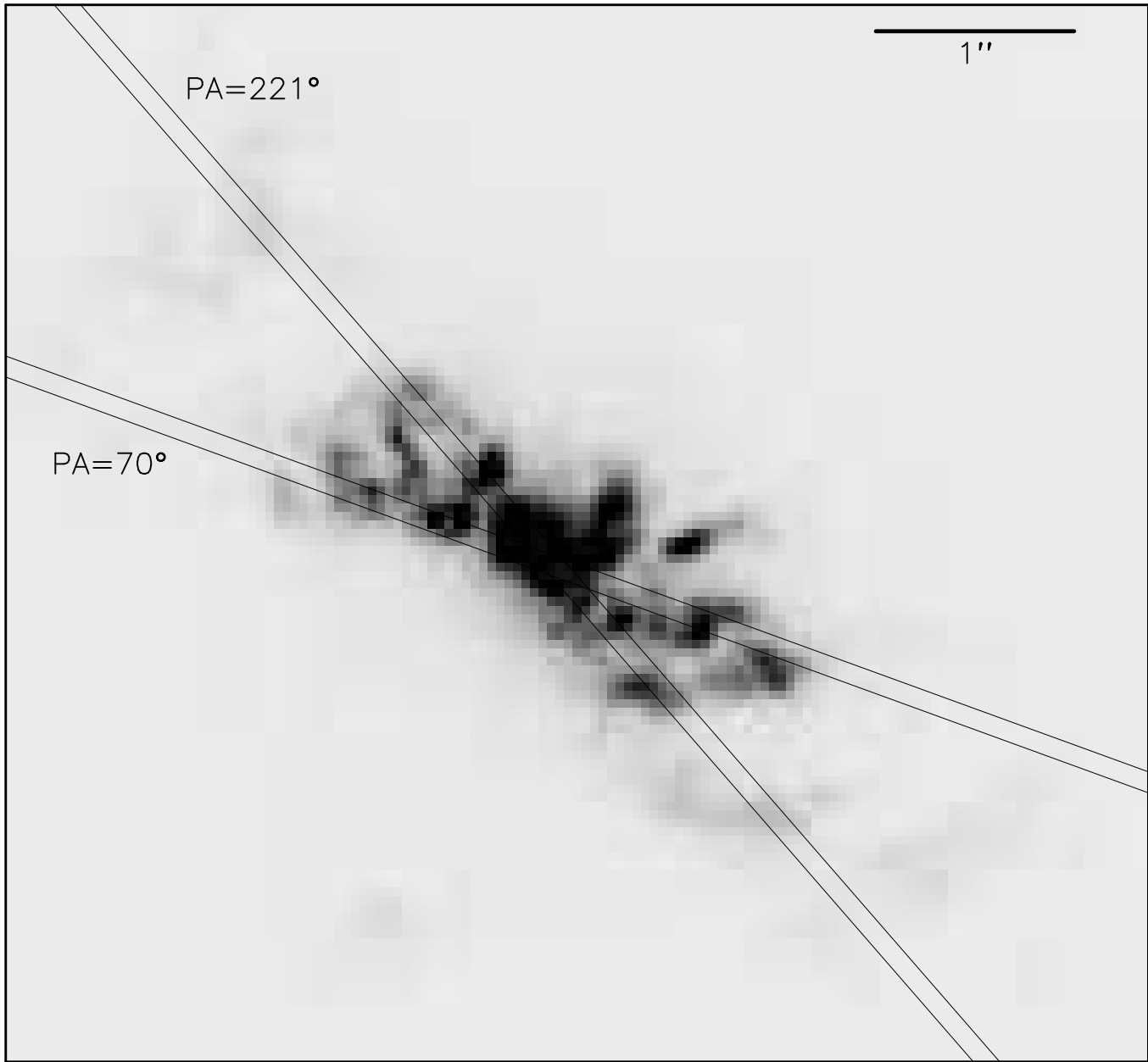
SW Side			NE Side		
Extraction	Knot ¹	Region ²	Extraction	Knot ¹	Region ²
0.1 – 0.3	–	–	0.1 – 0.3	–	–
0.3 – 0.5	26	N	0.3 – 0.5	1	–
0.5 – 0.7	23	–	0.5 – 0.7	–	–
0.7 – 0.9	–	–	0.7 – 0.9	10	H
0.9 – 1.1	22	–	0.9 – 1.1	10	–
1.1 – 1.3	–	–	1.7 – 1.9	4	–
1.3 – 1.5	–	–	1.9 – 2.1	4	–
1.5 – 1.7	25	–	2.1 – 2.3	4	–
1.7 – 1.9	25	–	2.3 – 2.5	5	–
1.9 – 2.1	25	–	2.5 – 2.7	5	–
2.1 – 2.3	25	–	2.7 – 3.0	–	–
2.3 – 2.5	–	–	3.1 – 3.3	–	–
2.5 – 2.7	–	–			
2.7 – 2.9	–	–			
2.9 – 3.1	–	–			
5.5 – 5.7	–	–			
5.7 – 5.9	–	–			
5.9 – 6.1	33	–			
6.3 – 6.5	37	–			

¹Kaiser et al. 1999, ² Hutchings et al. 1999

TABLE 4b
Cloud Identification P.A. 70°

SW Side			NE Side		
Extraction	Knot ¹	Region ²	Extraction	Knot ¹	Region ²
0.1 – 0.3	–	–	0.1 – 0.3	–	–
0.3 – 0.5	26	N	0.3 – 0.5	11,6	–
0.5 – 0.7	23	–	0.5 – 0.8	6	–
0.7 – 0.9	19	–	0.8 – 1.0	9,12	–
0.9 – 1.1	–	D, D'	1.0 – 1.2	12	–
1.1 – 1.4	16	–	1.2 – 1.4	–	–
1.4 – 1.6	16	–	1.4 – 1.5	–	–
1.6 – 1.8	–	–	1.5 – 1.8	3	–
1.8 – 2.0	–	–	1.8 – 2.1	3	–
2.0 – 2.2	–	–	2.5 – 2.7	14	–
2.7 – 2.9	18	–	2.7 – 2.9	–	–
2.9 – 3.1	18	–	2.9 – 3.1	–	–
			3.1 – 3.3	–	–
			3.3 – 3.5	–	–
			3.5 – 3.8	–	–
			4.2 – 4.7	29	–

¹Kaiser et al. 1999, ² Hutchings et al. 1999



NGC 4151

Fig. 1.— A continuum subtracted WFPC-2 F502N image of NGC 4151 is shown with the STIS longslit apertures superposed. North is up and East is at the left. The slit at P.A. 221° goes through the nucleus while the one at P.A. 70° passes $0''.1$ to the south.

FIGURE 2 — figure2.jpg

Fig. 2.— The fully reduced, scattering corrected images are displayed for the observations taken at P.A. 221° . The dynamic range displayed is the same for all frames and runs from zero for the white background to 2.0×10^{-16} ergs $\text{s}^{-1} \text{cm}^{-2} \text{\AA}^{-1}$ for black. The receding NE side of the galaxy is at the top.

FIGURE 3 — figure3.jpg

Fig. 3.— The reduced and scattering corrected images are displayed for the observations taken at P.A. 70° . The dynamic range displayed is the same for all images and runs from zero for the white background to 2.0×10^{-16} ergs $\text{s}^{-1} \text{cm}^{-2} \text{\AA}^{-1}$ for black. The receding NE side of the galaxy is at the top. Note that the G140L observations were not obtained for this orientation.

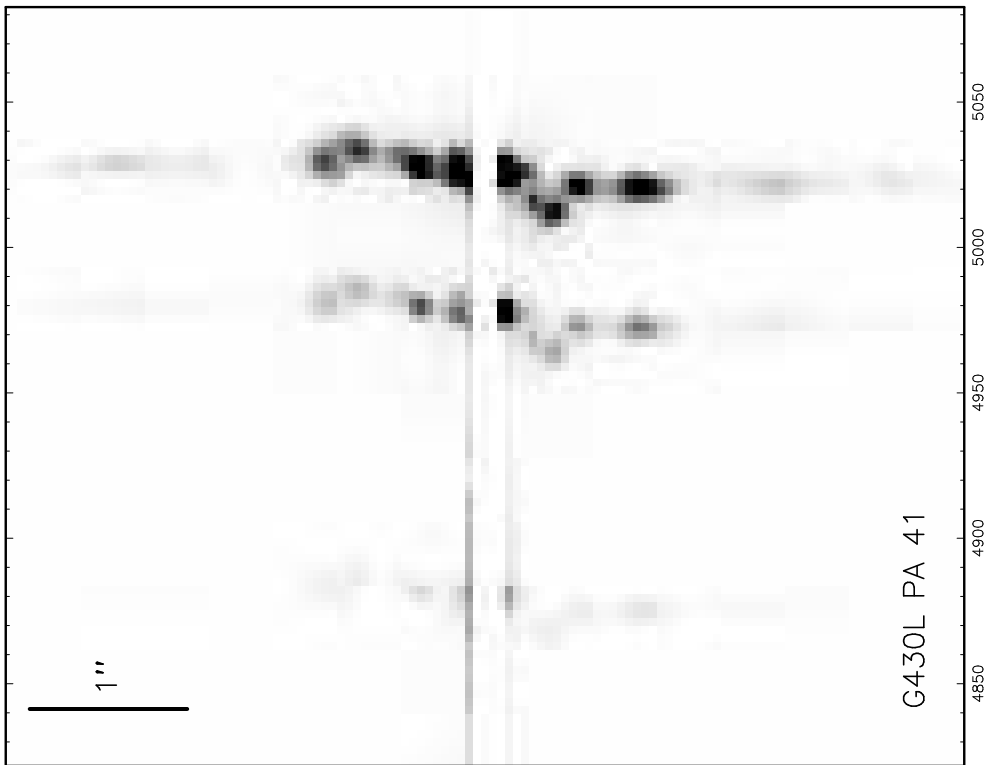
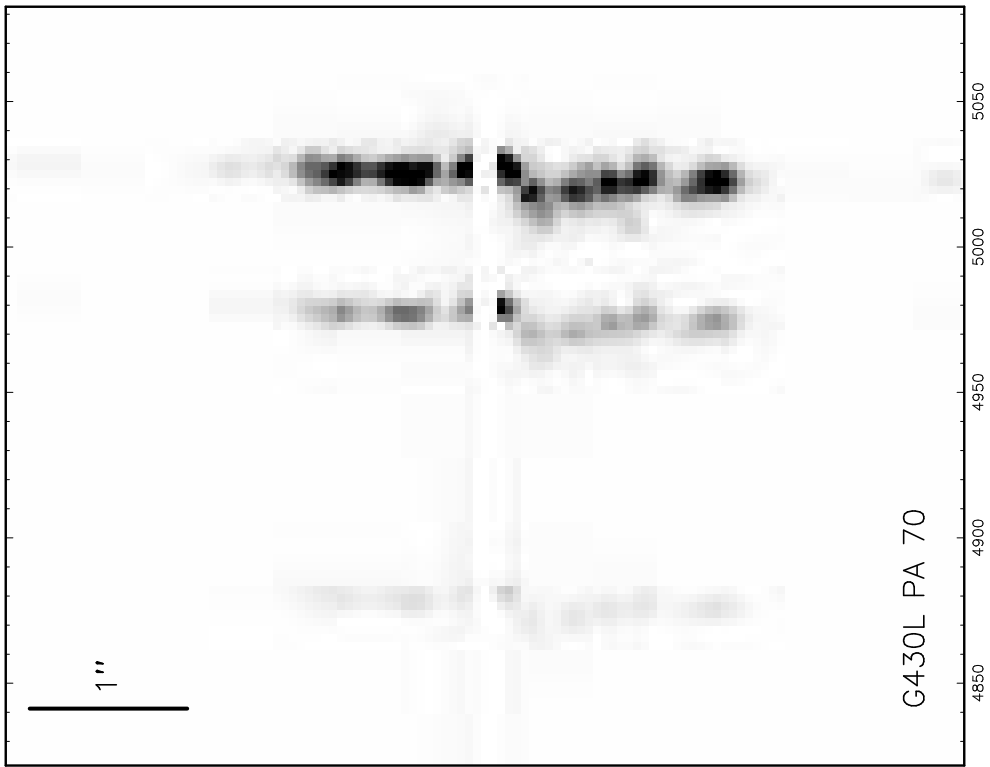


Fig. 4.— Portions of the longslit spectra centered on the $[\text{OIII}] \lambda 5007$, $[\text{OIII}] \lambda 4959$ and $\text{H}\beta$ lines for each slit position. As in Figures 2 and 3 NE is at the top.

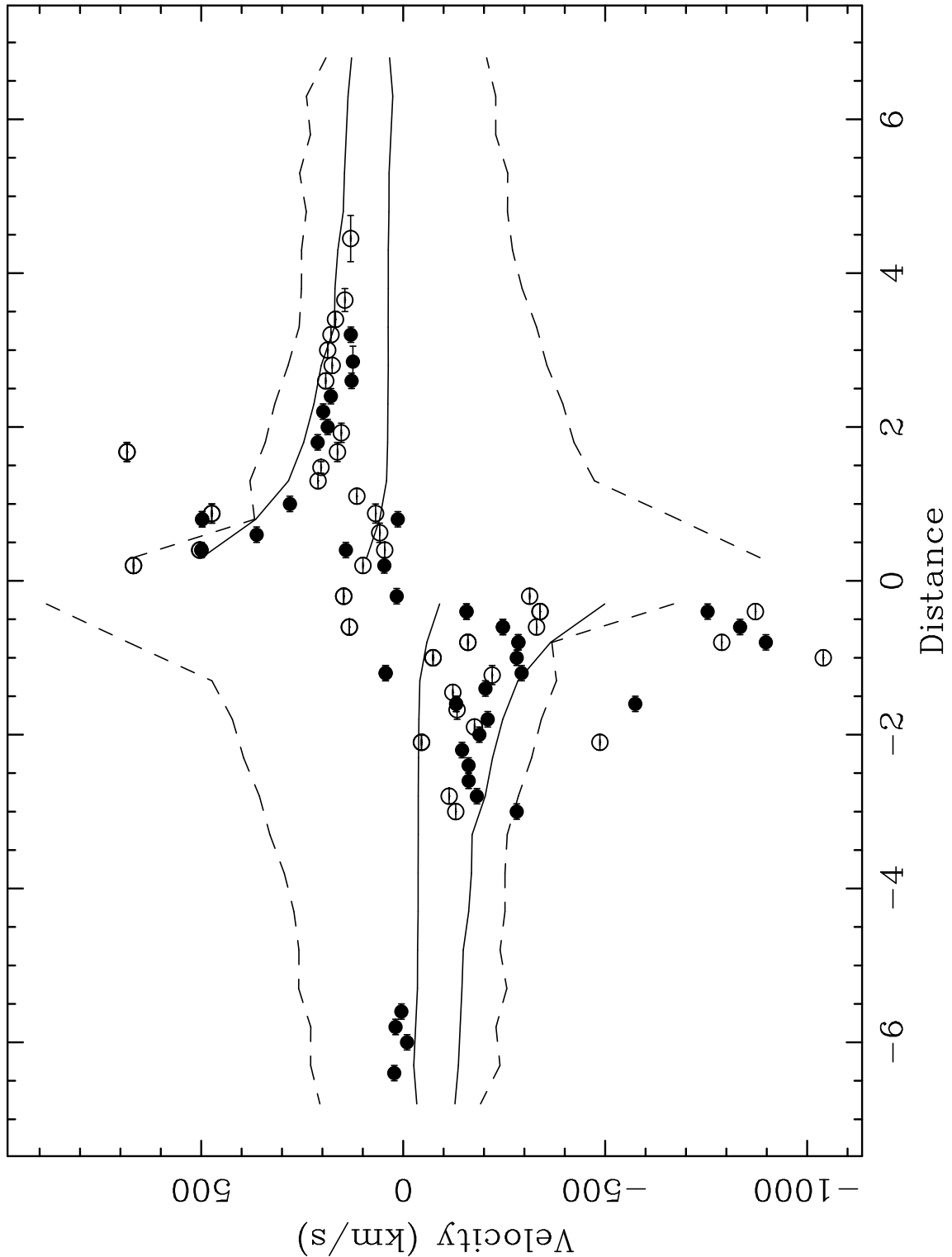


Fig. 5.— The velocities of the individual [OIII] $\lambda 5007$ components are plotted as filled symbols for points along P.A. 221° and as open symbols for points along P.A. 70° . The NE side of the slit is on the positive side while the SW side corresponds to the negative side. The uncertainties along the velocity axis are comparable to the size of the points plotted and the horizontal bars indicate the bin size of the extraction. The solid line shows the expected velocities in the case of a decelerating radial flow while the dashed line shows the case of a decelerating expansion perpendicular to the radio axis.

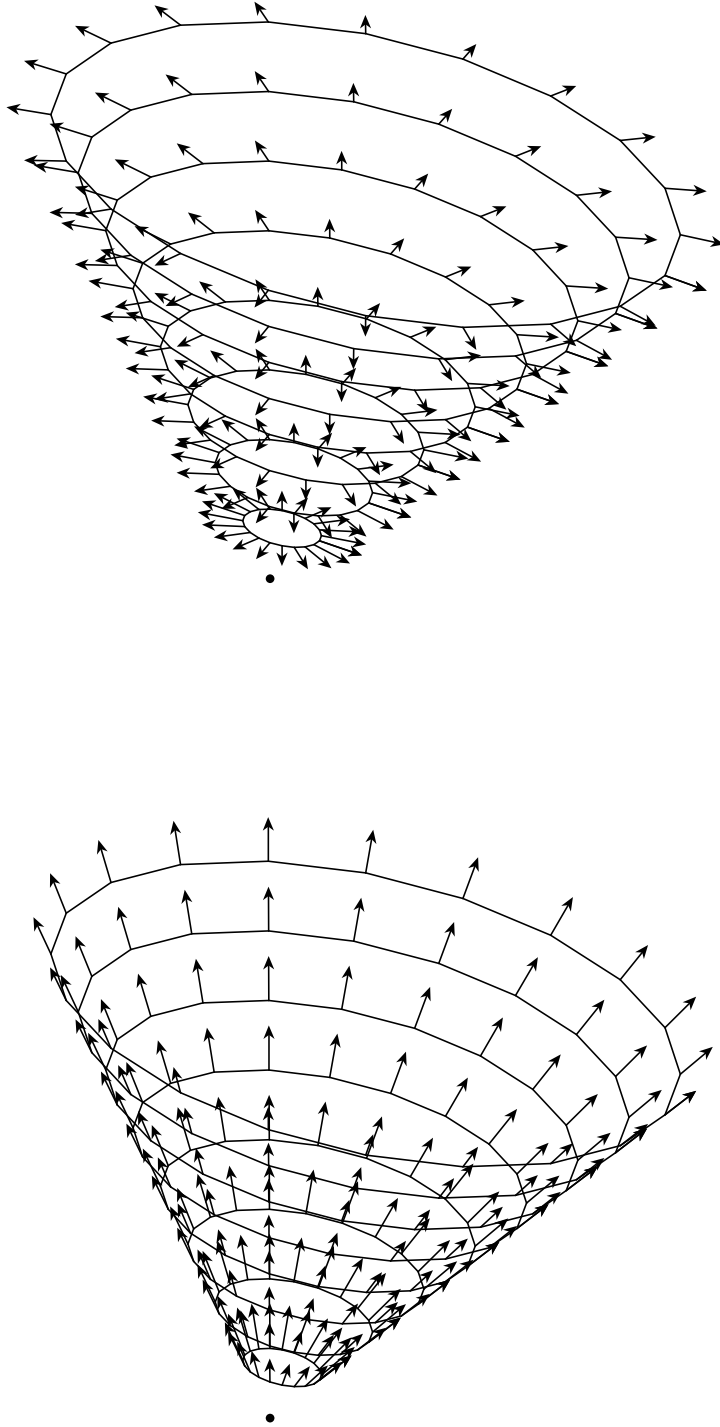


Fig. 6.— Examples of the model velocity fields are shown. We adopt the geometry of Pedlar et al. (1993), however our opening angle is smaller (70°) to better match the observed distribution of line emitting material. The the upper cone shows the case of a flow expanding in a direction perpendicular to the radio axis while the lower cone shows the case of a radial flow. Velocity vectors are shown for the outside surface of the cone.

FIGURE 7 — figure7.jpg

Fig. 7.— Our models can be used to produce artificial longslit emission line spectra. On the left we show a model emission line for the case of expansion away from the radio axis and on the right for a radial flow away from the nucleus. Models with constant velocity are shown at the top and for decelerating flows on the bottom.

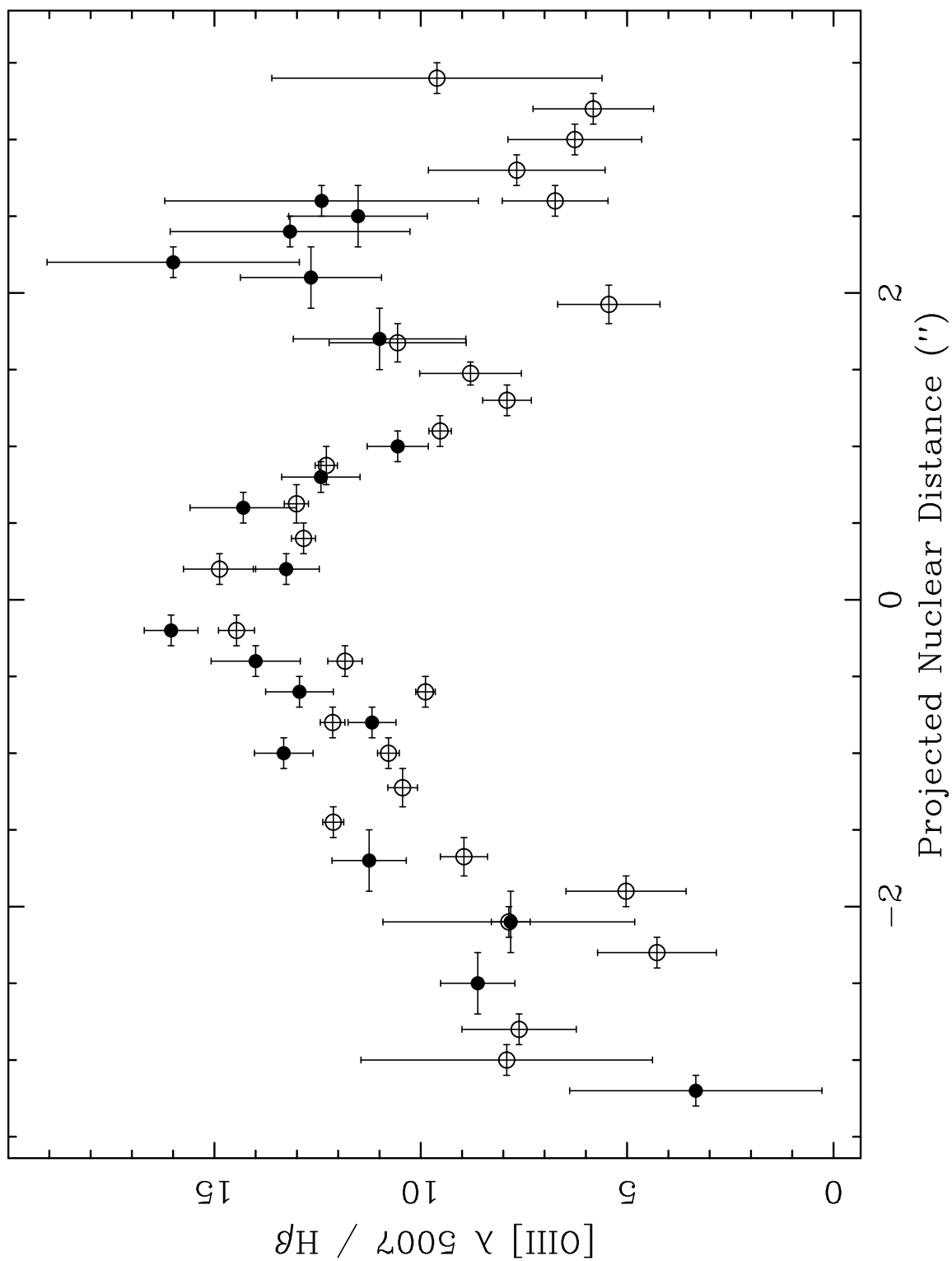


Fig. 8.— The ratio of [OIII] $\lambda 5007$ to $H\beta$ is plotted as a function of distance from the nucleus along the slit. Notice the trend for the ratio to decline with distance in the inner $2''$.

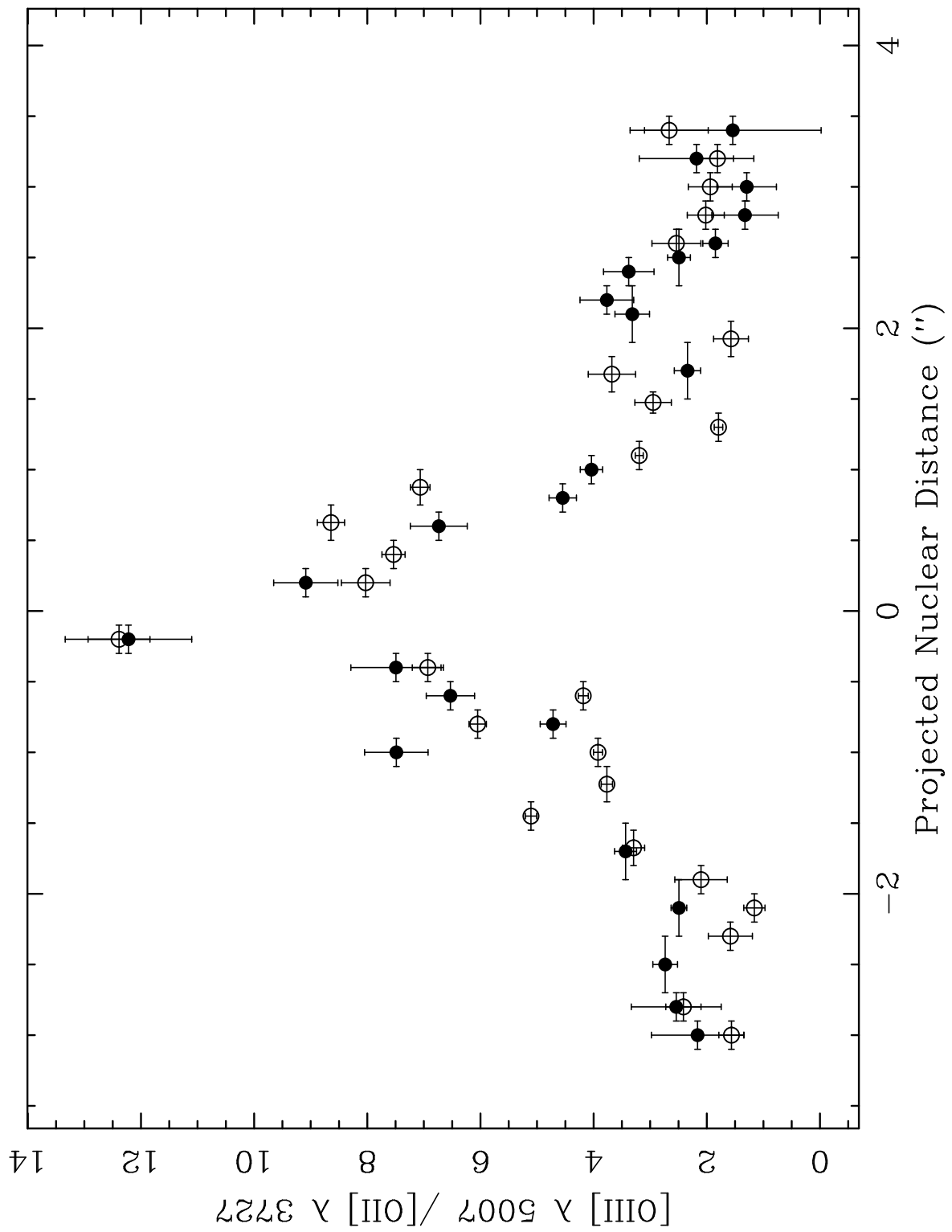


Fig. 9.— The ratio of [OIII] $\lambda 5007$ to [OII] $\lambda 3727$ is plotted as a function of distance from the nucleus along the slit.

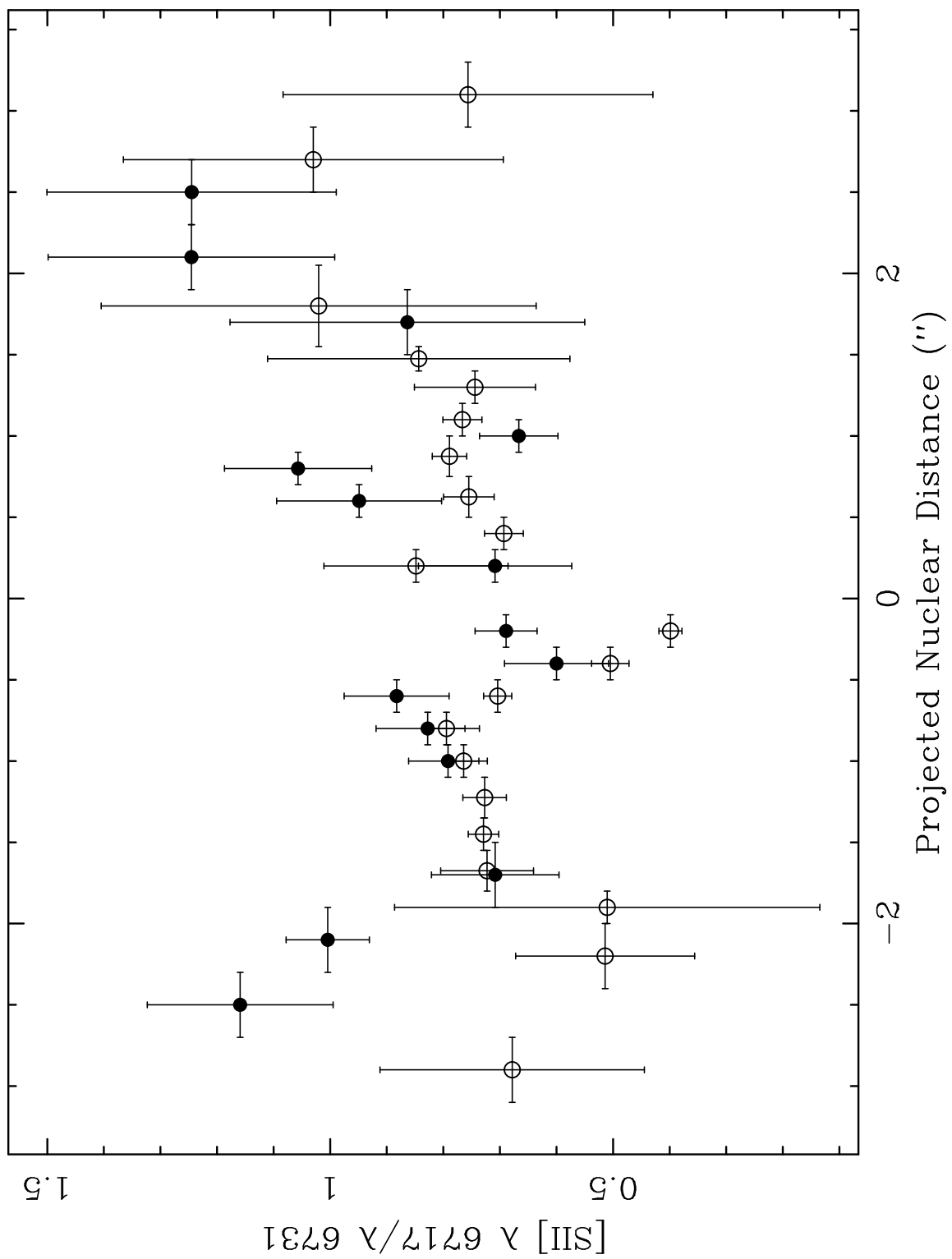


Fig. 10.— The density sensitive ratio $[SII] \lambda 6717 / [SII] \lambda 6731$ is plotted as a function of distance from the nucleus along the slit.

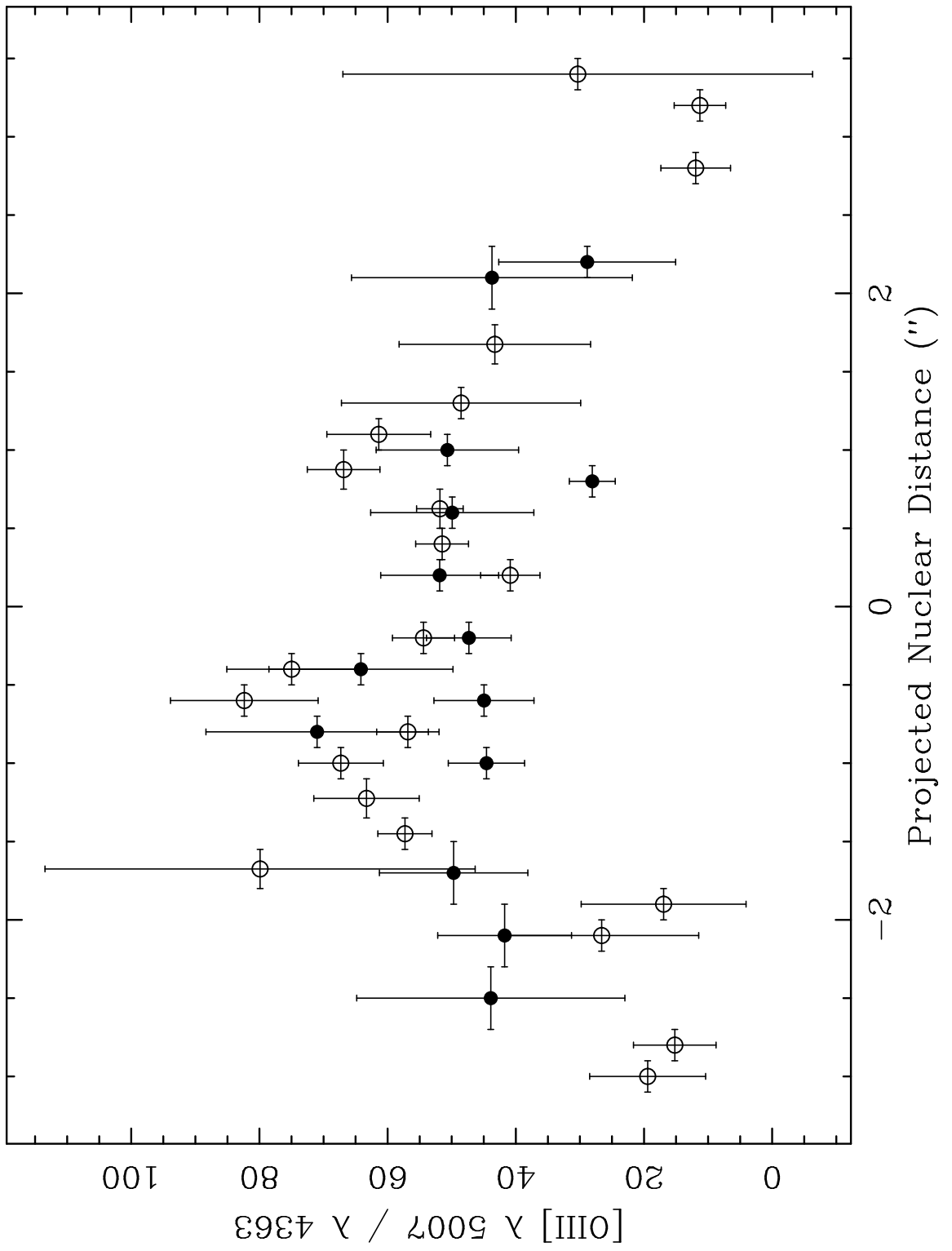


Fig. 11.— The temperature sensitive $[OIII] \lambda 5007 / [OIII] \lambda 4363$ ratio is plotted as a function of distance from the nucleus along the slit.

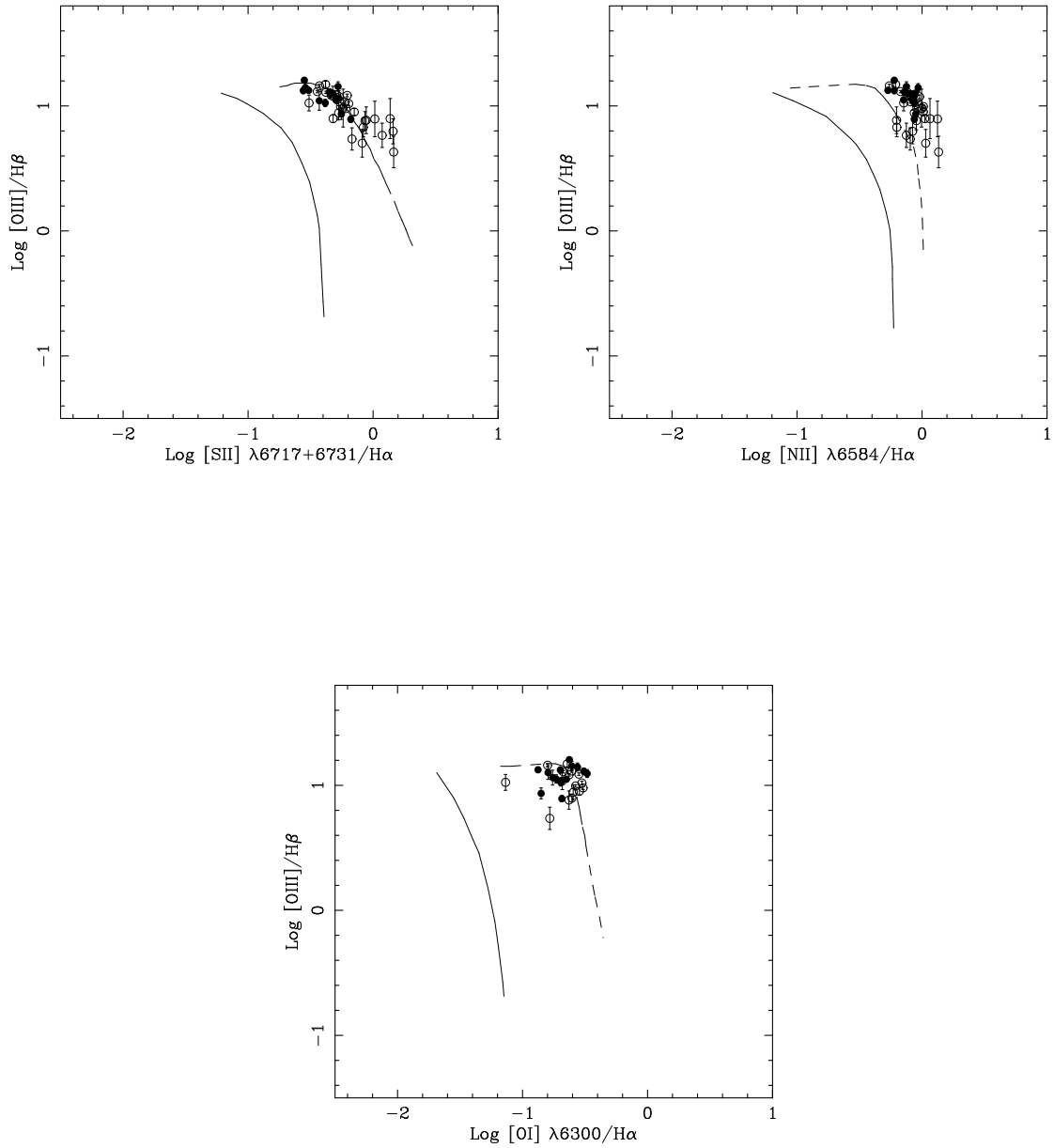


Fig. 12.— Standard optical emission line ratio diagrams are plotted: a, [SII] $\lambda 6717 + \lambda 6731$ vs. [OIII] $\lambda 5007 / \text{H}\beta$; b, [NII] $\lambda 6584 / \text{H}\alpha$ vs. [OIII] $\lambda 5007 / \text{H}\beta$; c, [OI] $\lambda 6300 / \text{H}\alpha$ vs. [OIII] $\lambda 5007 / \text{H}\beta$. In each diagram the solid line shows the line separating star-forming regions from AGN and the dashed line shows the photoionization models of Ferland and Netzer (1983) for solar abundance. The results show a compact distribution of points for the NGC 4151 NLR, suggesting uniform excitation for the ensemble of clouds.

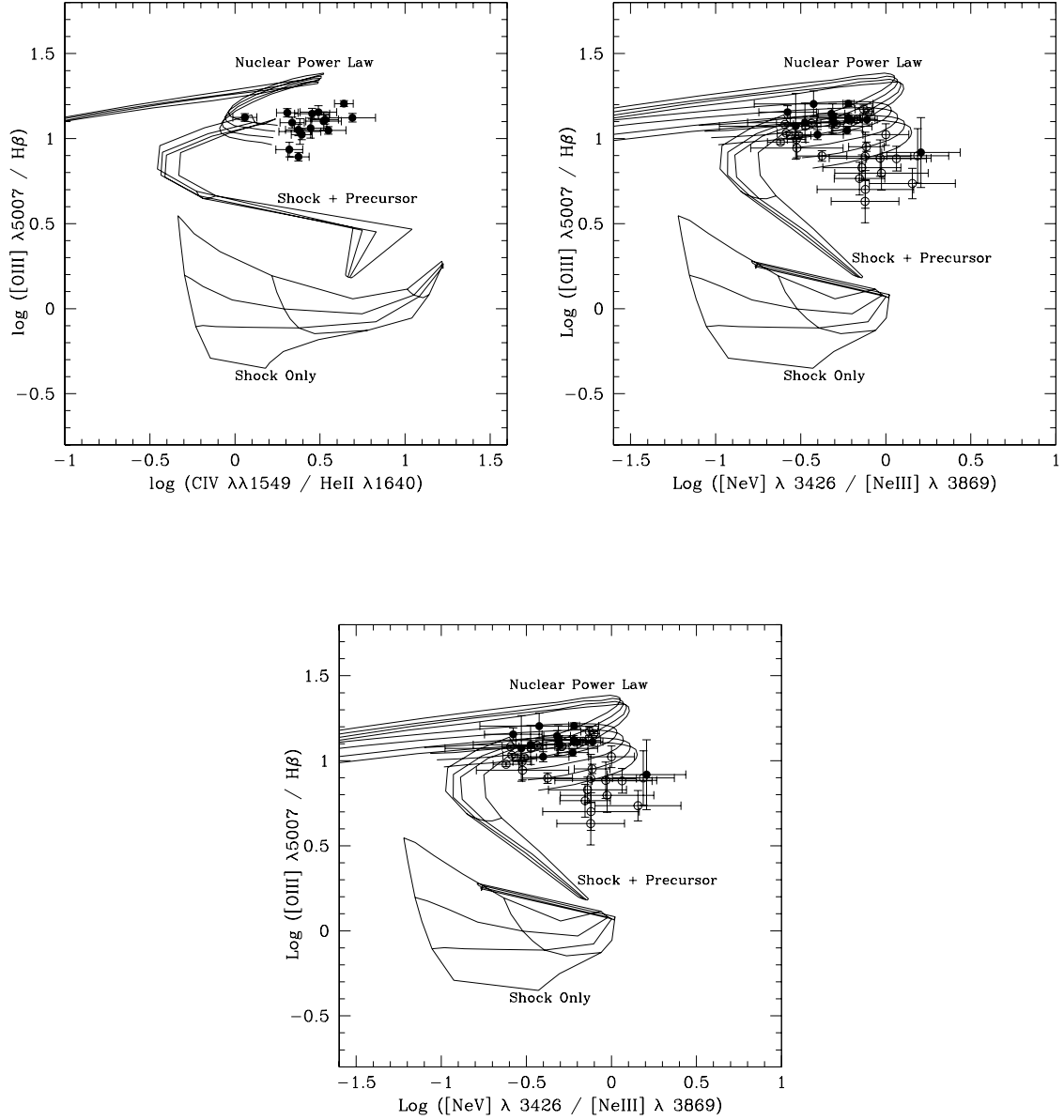


Fig. 13.— Emission line ratio diagrams in the ultraviolet and near ultraviolet including grids for shock ionization models, auto-ionizing shock models and power-law ionization models calculated using the MAPPINGS II code (Sutherland and Dopita, 1993, Allen *et al.* 1998). For the shock plus precursor models, the shock velocity increases from 200 km s^{-1} to 500 km s^{-1} moving from low to high $[\text{OIII}] \lambda 5007 / \text{H}\beta$ ratios. The power-law models are for index $\alpha = -1$ and $\alpha = -1.4$ ($f_\nu \sim \nu^\alpha$) and densities $n_e = 100 \text{ cm}^{-3}$ and $n_e = 1000 \text{ cm}^{-3}$. The ionization parameter for these models varies from roughly $U = 10^{-2.5}$ to $U = 1$ starting from the left hand edge of each diagram.

This figure "figure2.jpg" is available in "jpg" format from:

<http://arxiv.org/ps/astro-ph/9910019v1>

This figure "figure3.jpg" is available in "jpg" format from:

<http://arxiv.org/ps/astro-ph/9910019v1>

This figure "figure7.jpg" is available in "jpg" format from:

<http://arxiv.org/ps/astro-ph/9910019v1>